Differentiation of Static and Dynamic Interfacial Area in the Structured Packed Column

Chao Zeng[a], Yucheng Fu[a], Rajesh Singh[b], Jie Bao[b], Zhijie Xu[a]

[a]Physical and Computational Sciences Directorate, Pacific Northwest National Laboratory, Richland, WA 99352, USA

[b]Energy and Environment Directorate, Pacific Northwest National Laboratory, Richland, WA 99352, USA

Abstract:

Effective mass-transfer area plays a key role for post-combustion carbon capture. The static area, an inactive part relative to mass transfer, needs to be differentiated in the interfacial area. In the present study, CFD method is employed to investigate static and dynamic interfacial areas in Mellapak 500.Y structured packing. A wide range of physical properties and loading conditions are included to understand their effects on both areas. The result shows that the relationship between interfacial area and interfacial velocity at the local scale can be described by gamma distribution with good accuracy. The influences of various physical properties derived from simulation are compared with existing experiment-based correlations for both static and interfacial areas. The result shows the dominant influence of viscosity on the static area, and the most importance of the influence of contact angle on the interfacial area. This study also highlights the importance of viscosity, which is usually ignored.

Key words: static area, interfacial area, effective area, interfacial velocity, simulation

1. Introduction:

As global warming continues to be a primary concern, curbing CO_2 emissions has become an increasingly relevant topic in recent years. The flue gas from coal-fired power plants accounts for 30% of total U.S. CO_2 emissions (Rochelle, 2009). Thus, coal plants are endeavoring to incorporate capture technology into new facilities and to retrofit existing plant towers. Various capture strategies have been proposed. Chemical absorption, adsorption, cryogenics, membranes, and microbial/algal systems are among the frontrunners in this effort (Rao and Rubin, 2002). Of these, absorption with a chemical solvent is arguably the most mature and readily deployable

concept (Rao and Rubin, 2002). To achieve absorption, the flue gas flows countercurrent to the solvent through a packing material. Structured packing, made of corrugated sheets, has been cited as being a highly favorable option for use in the absorber, due to its superior performance relative to high mass-transfer efficiency and low pressure drop.

The capital costs of CO_2 capture are quite daunting because the absorber tower can be as large as 15 m in diameter. Performance evaluation and clear understanding of mass transfer is of vital significance for achieving a more efficient structured packing design before commercial deployment. Mass-transfer performance can be characterized by the product of mass-transfer coefficient and effective area. The effective area is the focal point of this research because an accurate prediction of the effective area is critically needed for the CO_2 capture by aqueous amine absorption.

The effective area (a_e) is where interfacial mass transfer takes place in a packed column. Note that the definition of effective area is different than wetted area (a_w) and interfacial area (a_i). Wetted area is the portion of the packing surface area covered with liquid, while the interfacial area is the total gas-liquid interface area. In structured packing, a portion of droplets is negligible at normal liquid loading (Rocha et al., 1993), and correspondingly wetted area and interfacial area are almost the same. The interfacial area can be divided into a static part (a_{st}) and a dynamic part (a_{dyn}) as $a_i = a_{st} + a_{dyn}$ (Puranik and Vogelpohl, 1974). The static part of the interfacial area is not renewed; after the saturation or depletion of the solute, it will no longer participate in the mass transfer. The dynamic part of the interfacial area is continuously renewed by the fresh solvent and thus remains active for mass transfer of solute. The difference between the static and dynamic parts can be discriminated by interfacial velocity because they each are defined by the hydrodynamic concept. The magnitude of the effective area depends on both absorption situations and hydraulic characteristics as $a_e = \chi(\mathrm{Ha}) \cdot a_{st} + a_{dyn}$ (Hegely et al., 2017), where Ha is the Hatta number that represents the ratio of chemical reaction to physical diffusion in a liquid film and χ(Ha) is a normalized coefficient as function of Ha, $\chi = f(\mathrm{Ha})$. Therefore, the clear differentiation of static and dynamic interfacial areas is important to accurately predicting the effective area. Measurement and prediction of the effective area have been the subject of many publications in the literature. De Brito et al. (1994) and Danckwerts (1970) reviewed the large variety of chemical absorption experiments to measure the effective area of interphase mass transfer in structured packings. Wang

et al. (2005) and Tsai (2010) performed an extensive review of effective area correlation for structured packing. However, most of these measurements and correlations interchangeably used the interfacial area to represent the effective area for column design, which would overestimate the mass-transfer area in most absorption situations (Puranik and Vogelpohl, 1974). Few studies differentiate static area and dynamic area to correlate the effective area. For example, Shi and Mersmann (1985) proposed a representative model on the basis of rivulet flow on an inclined flat plate. The correlation for wetted surface area is theoretically derived and then a correction factor is multiplied on wetted surface area to consider the difference between wetted area and effective area. The influence of static area is implicitly confounded by a correction factor, rather than explicit consideration. Rocha et al. (1996) developed an effective area prediction model and validated it with experiments conducted under different operating conditions. A factor of approximately 0.9 was also used to account for regions in packed bed that are not conductive to rapid surface renewal. The static area was also not explicitly considered. Puranik and Vogelpohl (1974) proposed a correlation for estimating effective area in evaporation and absorption, with and without chemical reaction. The influences of the static area and dynamic area are separately presented in the final correlation. It shows the dependence of static area on the ratio of the Weber number and Froude number. The effectiveness of static area for mass transfer is governed by a Hatta number-like dimensionless factor, which exhibits a relationship similar to that reported by Hegely et al. (2017). Joosten and Danckwerts (1973) also differentiated static area and dynamic area literally and attributed the effectiveness of the static area to an adsorption-dependent factor. The existence and effectiveness of static area also have been emphasized for effective mass transfer in the analysis of liquid holdup at different absorption conditions (Baldi and Sicardi, 1975; Gelbe, 1968; Patwardhan, 1979; Shulman et al., 1955). In all those studies, how to differentiate the static area from the total interfacial area is not clearly explained, leading to an unclear definition of static area. Because both static area and dynamic area are hydrodynamic concepts and related to local interfacial velocity, it is imperative to first analyze the relationship of interfacial velocity and interfacial area from which the static area can be determined by a threshold velocity. In combination with the chemical reaction condition, which will be analyzed in our next work, more accurate prediction of effective area can be obtained. A wide range of physical properties are analyzed to incorporate emergent solvents in hydrodynamic simulations. Therefore, the objective

of this study is to accurately quantify the percentage of static and dynamic interfacial area with various solvents and loading conditions in a structured packing column.

In practice, direct observation of local flow field within a packed column is a difficult problem to overcome (Basden et al., 2013; Green et al., 2007; Owens et al., 2009). Computational fluid dynamics (CFD) simulation can overcome this limitation and offers access to a wealth of data not available from experimental techniques. In this study, CFD simulation with the prevailing volume of fluid (VOF) method is employed to rigorously analyze the local interfacial velocity distribution. Sulzer Mellapak 500.Y structured packing is used as a base case in the simulation. Wetting of the structured packed column in an absorption column is quite complex and a large number of factors influence the interfacial area, such as solvent properties (surface tension and viscosity), packing surface characteristics (contact angle and roughness), operational condition (liquid load and gas load), packing design, etc. (Singh et al., 2018). The influence of these factors on the correlation of interfacial velocity and interfacial area is thus explored. A wide range of solvent viscosities and surface tensions are considered to incorporate new emergent solvents for carbon capture. In Section 2, the mathematical formation of the VOF method used in the CFD simulation is briefly introduced, as are the geometry and boundary conditions of the CFD packed column. The correlation of interfacial velocity and interfacial area relative to different influencing factors are discussed in Section 3. In Section 4, these results are compared with existing correlations for static area and interfacial area in the literature. The relative importance of different factors to both static area and interfacial area are evaluated as well, followed by concluding remarks.

2. Methodology

2.1. *Mathematical formulations*

Multiphase flow simulations of the hydrodynamics in Mellapak 500.Y packing were performed using the VOF method. The commercial CFD software, STAR-CCM+, was used to carry out the numerical simulations (CD-adapco, 2020). A brief outline of VOF method is provided here. The mass conservation and momentum equations are solved for a single fluid as follows:

$$\frac{\partial \rho}{\partial t} + \nabla \cdot (\rho \mathbf{u}) = 0 \tag{1}$$

$$\frac{\partial \rho \mathbf{u}}{\partial t} + \nabla \cdot (\rho \mathbf{u}\mathbf{u}) = -\nabla p + \mu \nabla^2 \mathbf{u} + \rho \mathbf{g} + \mathbf{F} \quad (2)$$

where p is pressure, $\mathbf{g}$ is gravity, μ is dynamic viscosity, and ρ is density. $\mathbf{F}$ is surface tension force at the gas-liquid interface, and $\mathbf{u}$ is the velocity vector of the fluid mixture. In the presence of gas and liquid phases, μ and ρ of the fluid mixture can be calculated as follows:

$$\rho = \alpha \rho_L + (1 - \alpha) \rho_G \quad (3)$$

$$\mu = \alpha \mu_L + (1 - \alpha) \mu_G \quad (4)$$

where α is the volume fraction of liquid phase and subscripts L and G denote the liquid and gas phase, respectively; and α is in the range of 0 and 1, where 0 denotes cell fully occupied by gas and 1 denotes cell fully occupied by liquid. The volume fraction α is solved by an additional transport equation as follows:

$$\frac{\partial \alpha}{\partial t} + \mathbf{u} \cdot \nabla \alpha = 0 \quad (5)$$

In Eq. (2), surface tension force at the gas-liquid interface is modeled as a volumetric force using continuous surface force model (Brackbill et al., 1992):

$$\mathrm{F_n} = -\sigma \nabla \cdot \left(\frac{\nabla \alpha}{|\nabla \alpha|} \right) \nabla \alpha \quad (6)$$

$$\mathrm{F_s} = (\nabla \sigma)_s |\nabla \alpha| \quad (7)$$

where σ is the interfacial tension and subscripts n and s denote normal and tangential components of a variable. The default normal direction is from liquid to gas. Because the constant surface tension coefficient is considered in this study, the tangential surface tension force $\mathrm{F_s}$ becomes 0. On the wall region, the $\frac{\nabla \alpha}{|\nabla \alpha|}$ in Eq. (6) is enforced as $n_w \cos \theta_w + s_w \sin \theta_w$. Herein, n_w and s_w are the unit normal and tangential vectors of the wall surface, respectively, and θ_w is the contact angle at the three-phase contact line. To acquire a sharp and clear interface, the high-resolution interface capturing (HRIC) scheme (Muzaferija, 1998) is used to reduce numerical diffusion. An additional convective term is added to Eq. (5) to increase the interface sharpness in the HRIC scheme.

2.2. *Problem setup*

High-resolution 3-D multiphase flow simulations were conducted to explore the hydrodynamics in a Mellapak 500.Y structured packed column that had two packing units. The packing geometry is shown in Fig. 1*a*. The geometry keeps the same as the PNNL laboratory continuous flow system absorber column which is developed by PNNL with a size small enough to be reproduced by the CFD model at a 1:1 scale (Fu et al., 2020b). The packed column has a radius of 3.82 cm and a height of 21 cm. A 0.1 mm radial gap is set between circular packing surface and column wall. This small gap is intended to reduce liquid flow along column wall surface which is the functionality of wiper band in practical packing column. It is noted that wiper band is not considered in this work. In industrial structured packing, wiper bands are present to redirect any liquid and vapor flowing along the wall back into the packing to ensure efficient contact between the two phases. Wiper bands shows observable effects on the pressure drop (Olujić, 1999) and local liquid distribution in proximity of wiper band, but limited liquid redistribution far away from wiper band (Basden, 2014). The height of each packing unit is 10 cm, and a 1 mm vertical gap is provided between them. When installing structured packing, the general industrial practice is to rotate each successive unit of packing 90° to promote liquid redistribution. The present CFD model follows a similar approach with the two units presenting an angle difference of $\theta_r = 90°$. A liquid distributor (small cylindrical tubes beneath the top surface in Fig. 1*a*) is installed at the top of the domain similar to industrial applications and the height of inlet tube is 0.5 cm. The gap between the distributor inlet and upper packing top surface is about 0.45 cm. Cai (2018) suggested a minimal drip point density for 500.Y of 160 /m^2. A total of 49 drip points is used to distribute the solvent uniformly across the packed column where the drip point density is more than the suggested value. The drip point distribution also influences the absorption efficiency and pressure drop in the structured packing (Pavlenko et al., 2020). To ensure uniform irrigation of solvent in the packing surface of the cylindrical column, a circular distribution of the drip points is favorable, as shown in Fig. 1*b*. Each drip point has diameter of 2 mm, and the liquid flow is vertically downward into the packed column. The velocity inlet boundary is specified at the liquid distributor as $u_{L,in} = u_L \cdot A/A_{in}$, where u_L is the liquid superficial velocity, A is the cross-sectional area of column, and A_{in} is the cross-sectional area of all dripping points. The bottom face has both outward solvent flow and inlet gas flow; it is not practical to set the gas phase boundary condition directly at the boundary (Fu et al., 2020a; Singh et al., 2020). Instead, the uniform gas velocity with the negative sign is specified at the remaining portion of the top face as $u_{G,out} = u_G \cdot A/A_{out}$, where u_G is

the gas superficial velocity and A_{out} is the area of the outlet boundary. The bottom of the column is specified as the outlet boundary condition for both liquid and gas phases in simulation. The wall of the column is set as having no-slip wall boundary conditions with a static contact angle. The surface of the packing sheets is specified as being a no-slip wall with a static contact angle as well.

Air and industry-used solvents for carbon capture are employed as the working fluids. The 20% monoethanolamine (MEA) was used as the base case, which has properties of μ_L = 1.18 cP, ρ_L = 996 kg/m^3, σ = 57.8 *m*N/m, and θ_w = 40° (Singh et al., 2017). The superficial velocities for the liquid and gas phases are u_L = 0.004 m/s and u_G = 0.05 m/s, respectively. The corresponding liquid load is 14.4 m^3/m^{2}h, in the manufacturer suggested operating range from 0.2 m^3/m^{2}h to 200 m^3/m^{2}h. The corresponding F-factor ($F = u_G\sqrt{\rho_G}$) for gas load is $0.06\sqrt{Pa}$, lower than loading point $F = 2.5\sqrt{Pa}$ from manufacturer. Both liquid and gas loads are in the low range of appliable loading for commercial column sizes. The small liquid and gas loads in this study is selected based on the capacity limitation of PNNL laboratory continuous flow system (Fu et al., 2020b). At high flow rate, the gear pumps may exceed maximal rated differential pressure (torque limited). To incorporate the new emergent solvents, a range of solvent properties and loading conditions are examined and listed in Table 1. In each simulation, one parameter was varied while keeping the remaining properties the same as the base case, which is highlighted in Table 1. In the following comparison with existing correlations, additional cases are run to increase the database of this study.

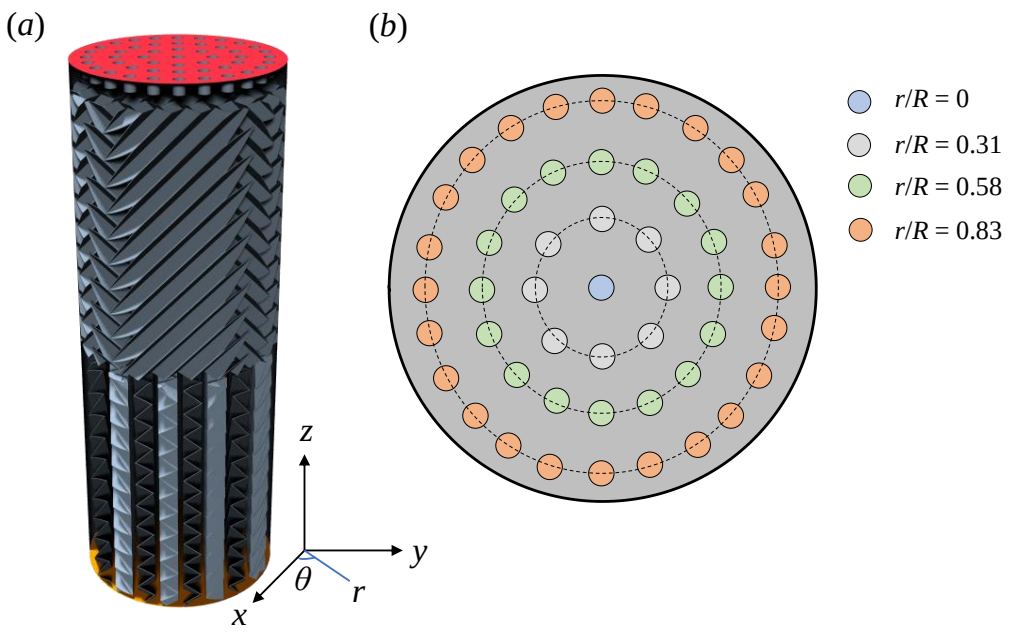

Fig. 1. (*a*) Configuration of two-unit Mellapak 500.Y structured packing columns used in the simulation. (*b*) The distribution of the dripping points of the liquid distributor at the top surface of the column.

Table 1. Range of solvent properties and operating conditions used in the simulations.

Parameters	**Values**
Liquid superficial velocity, u_L (m/s)	[0.001 0.003 **0.004** 0.0058 0.0085 0.0113]
Gas superficial velocity, u_G (m/s)	[0 0.002 0.02 **0.05** 0.08]
Static contact angle, θ_w (°)	[9 18 36 **40** 54 72]
Surface tension, σ (mN/m)	[10 15 20 25 30 38 52 **57.8** 66]
Liquid viscosity, μ_L (cP)	[**1.18** 2.31 3.72 6.54 9.36 12.18]
Rotation angle between two units, θ_r (°)	[0 18 36 54 72 **90**]

The computational flow domain is discretized by polyhedral mesh elements in the core volume. Because the solvent flows over corrugated sheets and the boundary wall in the structured packing, a prism layer mesh element is employed to resolve the boundary layers and the velocity gradient of the flow near the surface. The cross-sectional mesh configuration is shown in Fig. 2. A total of 7.5 million cells is generated in the computational domain. The packing surface and wall surface

204 is refined with the prism layer mesh. The prism layers each have a thickness of 1.2 mm and 10
205 layers. The CFD simulations were run on the Pacific Northwest National Laboratory high-
206 performance cluster. Each compute node has 24 cores, and each simulation ran on 8 nodes with
207 total 192 cores. An implicit unsteady solver was used for the time steps. All the cases were run for
208 10 s to ensure the interfacial area reached a pseudo-steady state.

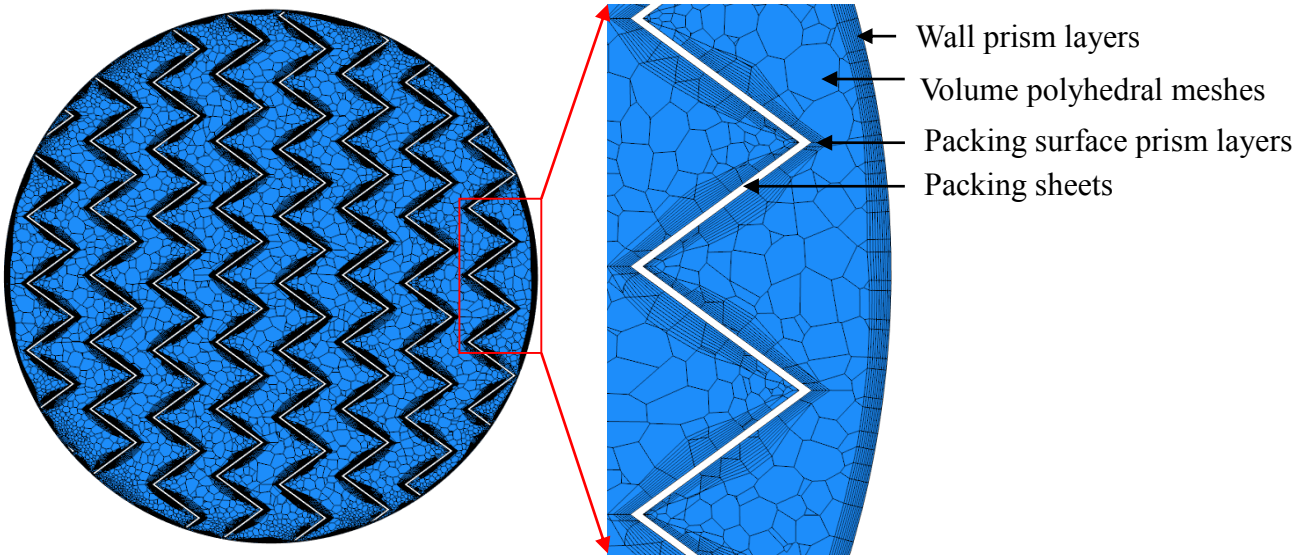

209

210 Fig. 2. Snapshot of the CFD mesh generated in the computational domain.

211 2.3 *Mesh independence study*

212 A mesh independence test was conducted to ensure there was an optimum number of cells in the
213 computational domain for economic simulations. The base case was run with six mesh sizes. The
214 evolution of the interfacial area in the packing column was monitored. Note that liquid film on
215 column wall was excluded in the calculation of a_i. The fractional area is defined as the ratio of
216 interfacial area to the geometric area, $a_f = a_i/a_p$. The transient fractional areas are plotted in Fig. 3.
217 All simulations achieved a pseudo-steady state value of a_f at about 6 s. The calculated a_f reduces
218 when using a finer mesh and finally remains unchanged. Because the VOF method requires finer
219 mesh near the gas-liquid interface, the coarse mesh is likely to have marked diffusion at the
220 interface and consequently account for more cells. The results at the 7.5 million mesh size can be
221 regarded as accurate at an affordable computational cost. Therefore, 7.5 million mesh cells will be
222 used for all simulation cases in the following analysis.

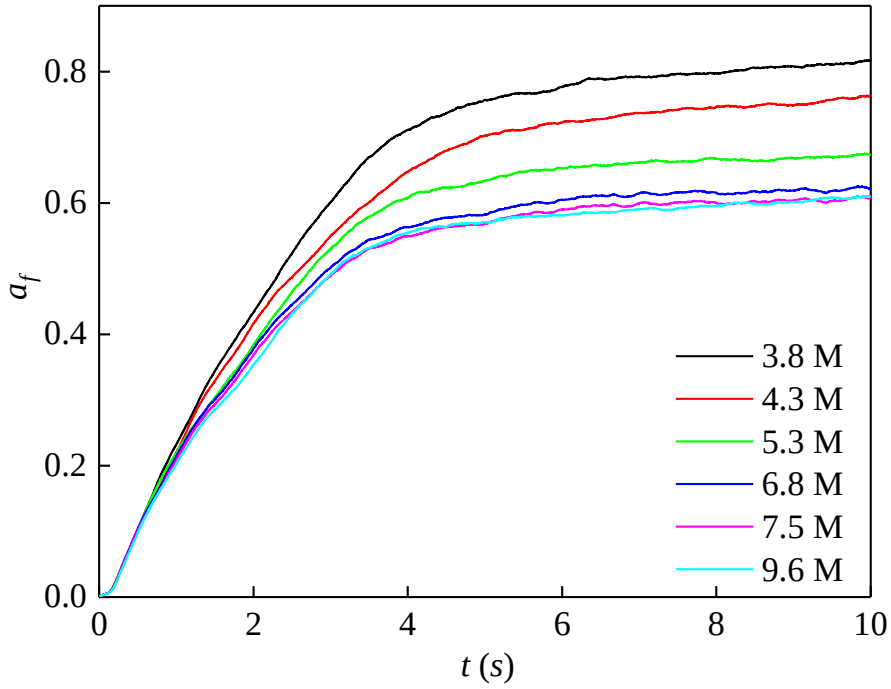

Fig. 3. Fractional area with respect to simulation time at different mesh size resolutions. The simulations are run under the base case condition.

3. Results

The transient flow development for the base case is depicted to show the distribution of the solvent in structured packing. The fractional area at the pseudo-steady state is correlated with the interfacial velocity of the base case. The ratio of static interfacial area is described using the gamma distribution. Then, the effects of solvent properties and operating conditions on the total area and static interfacial areas are analyzed.

3.1 *Transient flow development*

The temporal evolution of the liquid-gas interface inside the packed column is illustrated in Fig. 4. This temporal evolution of the fractional area corresponds to the magenta curve (7.5 M) in Fig. 3. The liquid-gas interface is shown with the coloring indicating the local interfacial velocity. In the beginning, the solvent flows downward from the distributor and reaches the bottom in about 3.0 s. This corresponds to the initial sharp increasing segment of the curve shown in Fig. 3. The solvent film spreads more uniformly on the bottom until about 5.0 s. After that, the flow reaches the pseudo-steady state and exhibit a nearly constant interfacial area. Note that the large rivulet

flow strip seen in the image is located on the column wall, which provides a non-trivial additional interfacial area for the small size columns.

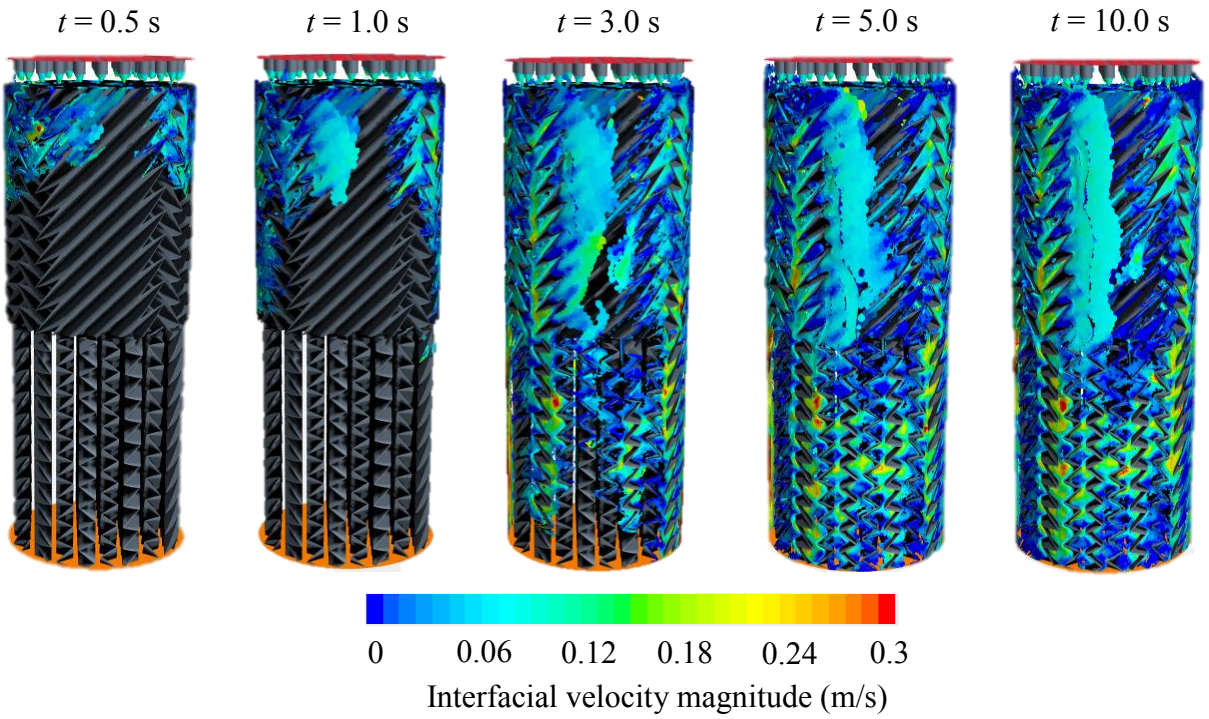

Fig. 4. Temporal evolution of the liquid-gas interface from 0 to 10 s. The liquid-gas interface is colorized by interfacial velocity magnitude.

3.2 *Interfacial area of the base case*

The interfacial velocity is used to differentiate the static and dynamic interfacial areas. Therefore, the relationship between the interfacial area and interfacial velocity is investigated first for the base case. The interfacial area and interfacial velocity magnitudes at t = 10 s in Fig. 4 are extracted from the simulation, excluding the liquid film on the column wall. The interfacial velocity is normalized by superficial liquid velocity and the range is discretized into a series of sections. The cumulative fractional area is normalized to the range of 0 to 1. The cumulative density function (CDF) of the fractional area with respect to normalized interfacial velocity is plotted in Fig. 5*a*. The gray cumulative histogram shows the simulation data. This CDF from the simulation is fitted by the CDF of the gamma distribution. The corresponding probability density function (PDF) of the

fractional area with respect to normalized interfacial velocity is illustrated in Fig. 5b. The CDF and PDF of the gamma distribution, respectively, are

$$F(x) = \frac{c}{\Gamma(a)}\gamma\left(a, \frac{x}{b}\right) \tag{8}$$

and

$$f(x) = \frac{c}{\Gamma(a)b^a}x^{a-1}e^{-x/b} \tag{9}$$

where $\Gamma(\cdot)$ is the gamma function, $\gamma(\cdot,\cdot)$ is the lower incomplete gamma function. a and b are the shape and scale parameters of gamma distribution, respectively. c is a coefficient to match the fitting results. The fitted CDF and PDF of the gamma distribution are blue lines in Fig. 5. Both show a good match with associated simulation data with the coefficient of determination equal to 1.0, and the minor difference is located at middle and end segments of the histogram. The merit of the CDF display lies in the clear correspondence of cumulative fractional area and certain interfacial velocity. It can be easily applied to estimate the portion of static interfacial area in the interfacial area.

There is no existing clear definition of static area in the literature, even though this concept is widely used to denote the stagnant region in the column. In this study, the static area is defined based on the contribution of specific liquid region to overall mass transfer performance in packing column. The volumetric mass transfer coefficient in column can be expressed as (Song et al., 2018)

$$k_g' \cdot a_e \approx \frac{u_L}{hRT}\ln\left(\frac{C_{CO_2,in}}{C_{CO_2,out}}\right) \tag{10}$$

where k_g' is the liquid film mass transfer coefficient, h is the height of the packing column, R is ideal gas constant, T is temperature, $C_{CO_2,in}$ and $C_{CO_2,out}$ are the inlet and outlet CO_2 concentration in the column. Eq. (10) calculates the average mass transfer coefficient in packing volume based on the superficial liquid velocity. If the liquid region with interfacial velocity u_i has higher velocity than u_L, that region contributes more than average to the overall mass transfer; conversely at u_i/u_L <1, that region contributes less than average to the overall mass transfer. Therefore, static area is defined as the liquid area with interfacial velocity following $u_i/u_L < 1$. It is noted that this definition is from aspect of overall mass transfer performance, rather than local hydrodynamics.

In what follows, $u_i/u_L = 1$ will be used as a critical velocity to differentiate the low and high velocity regions. For example, the static area in the interfacial area is $a_{st}/a_i = 0.056$ for the base case. In addition, the relative weights of different interfacial velocities in the fractional area are also represented by the CDF display. For the gamma function fitting, the potential implication of Eq. (8) lies in the prediction of the static and dynamic areas if the critical velocity is determined. In addition, the parameters' product $a \times b$ in the gamma distribution reflects the mean interfacial velocity in the column, and it is 11.83 (normalized) for the base case locally, because it is collected from individual interface cells. However, there is another widely used way to calculate the average interfacial velocity from global sense. The average interfacial velocity from global sense, denoted as $\bar{u}_i$, can be calculated by liquid load, as follows:

$$\frac{a_w}{h} \times \delta_L \times \frac{2}{3}\bar{u}_i = u_L \times A \tag{11}$$

where a_w/h denotes the cross-sectional perimeter of the liquid film. δ_L is mean film thickness, and it can be estimated from Nusselt theory (Bird et al., 2006), $\delta_L = \left[\frac{3\mu_L u_L}{\rho_L \cdot g \cdot a_p}\right]^{1/3}$. $\frac{2}{3}\bar{u}_i$ is average velocity of the liquid film where factor 2/3 comes from the conversion between mean velocity and maximum velocity assuming parabolic velocity profile in liquid film. For the base case, a_w = 0.2678 m^2, h = 0.2 m, and δ_L = 0.143 mm. Therefore, normalized interfacial velocity $\bar{u}_i/u_L$ is 48.15. Note that this calculation assumes the uniform liquid thickness for all interfacial velocity rather than the area-weighted average interfacial velocity. This normalized interfacial velocity is closer to the median of interfacial velocity range, which is equal to 37.8. The interfacial area-weighted interfacial velocity is calculated from local interface and can represent the local interfacial velocity in packing column, whereas the mean average velocity from Nusselt theory is calculated based on assumption of uniform liquid thickness and cannot represent the real average velocity very well. The noticeable discrepancy between the liquid film thickness of the Nusselt theory prediction and the experimental result is also validated by Schug and Arlt (2016).

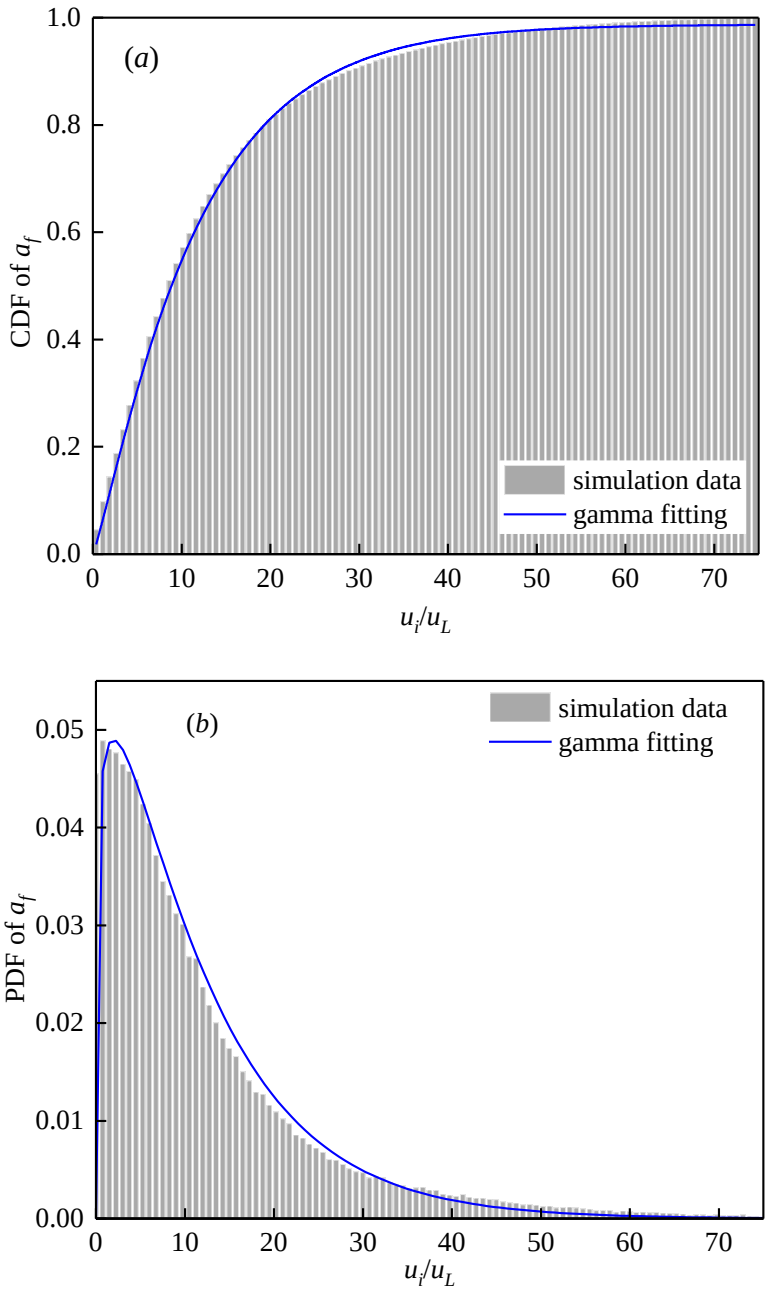

Fig. 5. (a) Cumulative density function and (b) probability density function of the fractional area with respect to normalized interfacial velocity. The gray bars signify the simulation results, and the blue line denotes the CDF and PDF fitting curve with gamma distribution, respectively.

3.3 *Effect of viscosity*

With industrial use of new solvents, a wide range of viscosities needs to be included to cover general situations. The influence of μ_L on mass-transfer efficiency is extensively explored mainly

by using the interfacial area and mass-transfer coefficient (Nakajima et al., 2000; Rizzuti et al., 1981; Song et al., 2018). In contrast to those analyses, the approach presented here incorporates interfacial velocity distribution at the local scale. The correlations of a_f and u_i at six μ_L values presented in Table 1 are analyzed, as shown in Fig. 6*a*. The curves in Fig. 6a are generated by fitting simulation data with gamma distribution Eq. (8). The coefficients of determination are all above 0.99 for the fitting. Fig. 6*a* shows the steeper slope of the CDF curves at the beginning with higher liquid viscosity, indicating more interfacial areas are associated with lower interfacial velocity. This is also verified by the mean interfacial velocity trend with respect to viscosity shown in Fig. 6b. The mean interfacial velocity decreases from 11.83 at μ_L = 1.18 cP to 6.28 at μ_L = 12.18 cP. It becomes harder for solvent to spread out on the corrugated sheet, leading to smaller interfacial areas. In terms of the static area, the ratio to interfacial area increases from 0.056 at μ_L = 1.18 cP to 0.371 at μ_L = 12.18 cP. Because one of the main goals of the design optimization of new packing is the elimination of stagnant liquid pools (Hegely et al., 2017), the solvent that has the higher viscosity needs special attention to increase the effectiveness of the static area or reduce the percentage of static area.

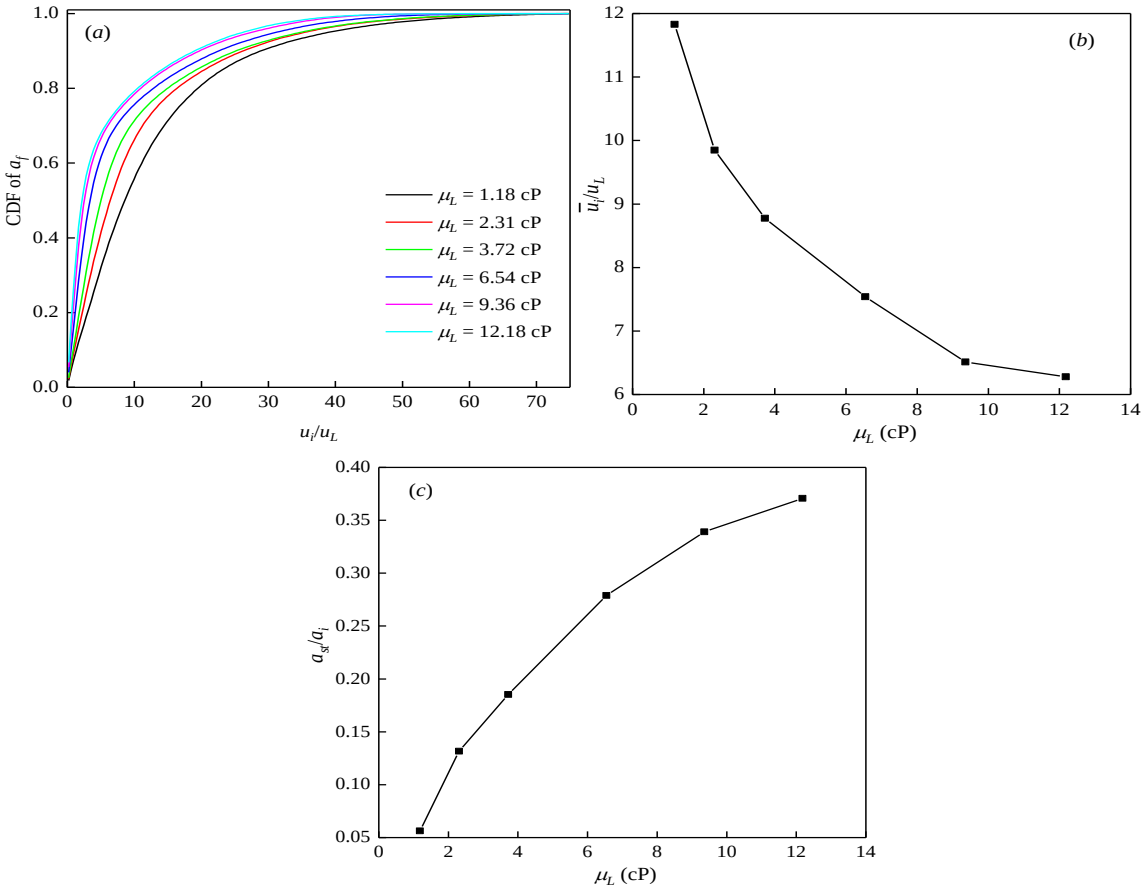

Fig. 6. The effect of viscosity on the (a) correlation of interfacial area and interfacial velocity, (b) mean interfacial velocity, and (c) ratio of the static area to interfacial area.

3.4 *Effect of surface tension*

The correlations of fractional area with interfacial velocity at different surface tensions are presented in Fig. 7a. Because nine cases listed in Table 1 have nearly overlapping curves, only four curves are shown for clarity purposes. The surface tension overall has a small impact on the fractional area distribution. The curves also cross over each other at different interfacial velocities, which is different from what is shown in Fig. 6*a*. The variation of the mean interfacial velocity with surface tension is shown in Fig. 7b. The figure shows the nonmonotonic variation within the range of 2.5 (difference between 1st data point and 6th data point), which indicates the small influence of surface tension on mean interfacial velocity. It is noted that the variation in Fig. 7b is mainly caused by interfacial velocity distribution change at different surface tensions in Fig. 7a.

The HRIC scheme to capture interface may be also partially contributable to the interface velocity change. The ratio of static area in interfacial area is shown in Fig. 7c. It is noted that both static area and interfacial area change at different surface tensions. The static area ratio is almost constant at lower surface tension values and increases at higher surface tensions. This can be explained by the effect of surface tension on the solvent flow in the structured packing. Gravity and surface tension are in direct competition with each other for area generation. Gravity serves to spread the liquid by pulling it toward and over the packing ridge, while surface tension acts to prevent the liquid from spilling over the packing ridge. At higher surface tensions, the flow resistance is larger and leads to the development of a larger percentage of static area. This trend in static area growth is also validated by the CFD simulation conducted by Basden (2014). It is also consistent with the empirical relationship of the static area reported by Puranik and Vogelpohl (1974), who showed that static area is positively proportional to surface tension. Tsai (2010) showed that a reduction in surface tension leads to an increase in interfacial area. This statement is also verified by our simulation results. Fig. 7c presents the ratio of static area in interfacial area, not the fractional area. Therefore, higher surface tension reduces the fractional area and increases the percentage of static area.

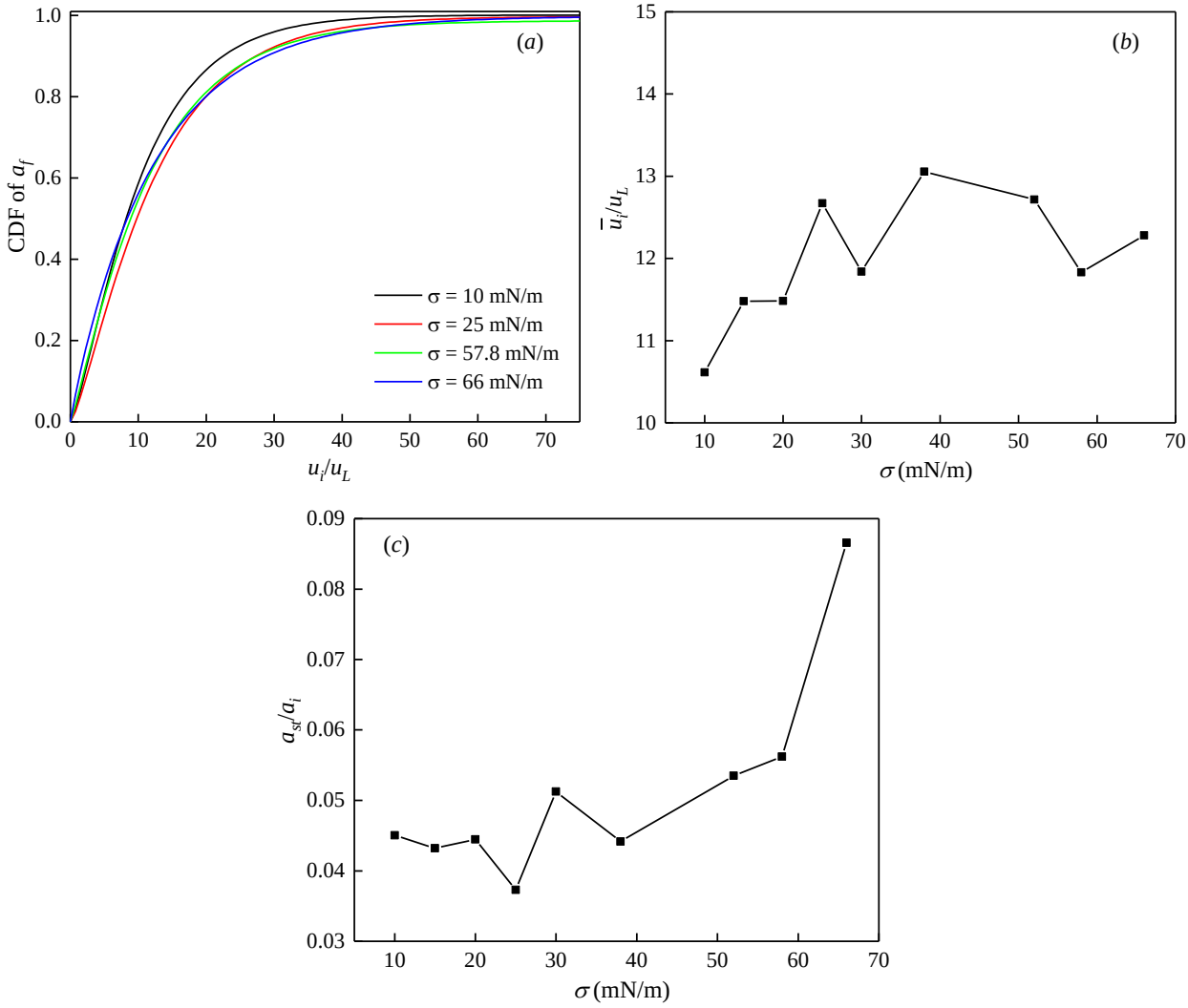

Fig. 7. The effect of surface tension (a) on the interfacial area and interfacial velocity, (b) on the average interfacial velocity, and (c) on the ratio of static area in interfacial area. To better illustrate the effects, only four curves are shown in (a).

3.5 *Effect of contact angle*

The contact angle is an important component of the system that indicates the degree of wetting when a liquid and solid interact. Young's equation reveals a relationship between the contact angle and interfacial tension of three phases. The packing sheets are generally manufactured from different materials such as ceramics, metal, and plastics, which have different contact angles for a given solvent. For a given packing surface, the contact angle and liquid-gas surface tension are inherently coupled. That is, $\cos\theta_w$ and σ follow a linear relation. Any changes in the surface tension

must be met with corresponding changes in the contact angle (Nicolaiewsky and Fair, 1999; Tsai et al., 2008). The effect of this coupling relationship is discussed below.

The effects of contact angle on the fractional area at intermediate surface tension (57.8 mN/m) and low surface tension (25 mN/m) are shown in Fig. 8*a* and Fig. 8*b*, respectively. Both plots show steeper curves at the low contact angle values. This means there is a large percentage of fractional area within a relatively low interfacial velocity. This is demonstrated by the mean interfacial velocity in Fig. 8*c*. A lower contact angle corresponds to a lower interfacial velocity. This trend can be explained by the effect of the contact angle on the flow morphology. The contact angle primarily determines if the liquid flows as a film or a rivulet (Basden, 2014). For the highly wetting case (9°), liquid flows primarily as a film. For the weakly wetting case (72°), liquid flows primarily as a rivulet, leading to a smaller wetted area. Because the liquid load is the same for various contact angle cases, Eq. (11) qualitatively shows a higher mean interfacial velocity as the wetted area decreases, even though the quantitative analysis by Eq. (11) shows significant deviation. Therefore, the lower contact angle shows a lower interfacial velocity for both surface tensions. Fig. 8c also shows that at a lower contact angle (<40°), the mean interfacial velocity at two surface tensions present a 1% difference, whereas this difference reverses at a higher contact angle (>40°). Because this small difference (~1%) is within the fluctuation range of the mean interfacial velocity at various surface tensions shown in Fig. 7b, this small difference is most likely a fluctuation that has a different surface tension, rather than a physical trend. The ratio of static area in interfacial area shows a monotonic trend with the contact angle (Fig. 8d). Because lower contact angle has better wettability, the solvent can spread over the packing ridge and presents a thin film near the ridge. Whereas at a higher contact angle, the solvent mainly flows in a valley as rivulet flow that has a larger thickness (Singh et al., 2017). Thin film has a lower interfacial velocity than that of a rivulet at the same liquid load. Therefore, the simulation with the lower contact angle has a higher ratio of static area. In addition, the lower surface tension has a smaller ratio of static area, which is consistent with Fig. 7c. The ratio change in static area for both surface tension (Fig. 7c) and contact angle (Fig. 8d) is around 5%, which indirectly demonstrates the similar effects of contact angle and surface tension on the static area.

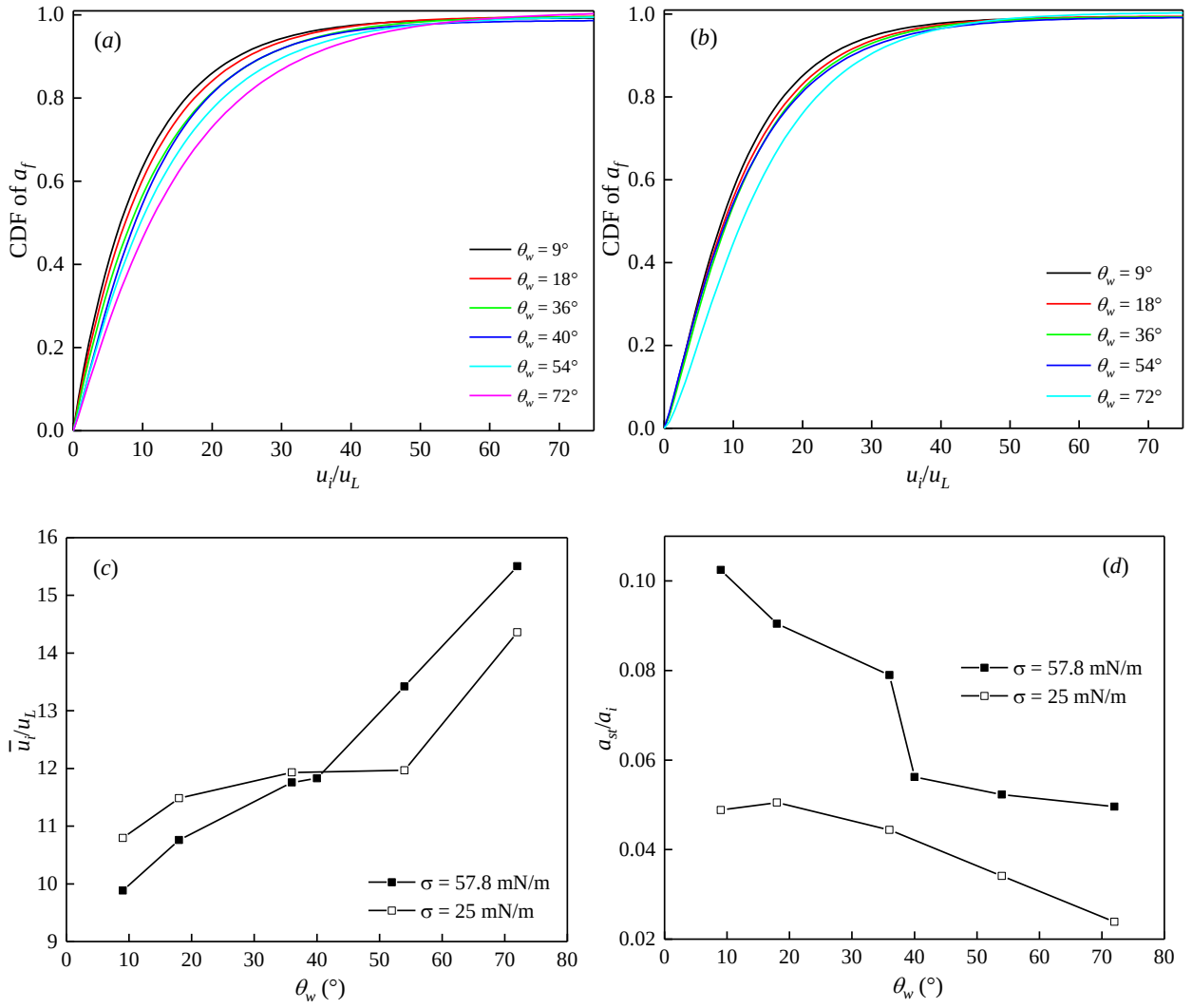

Fig. 8. The effect of contact angle (a) on the correlation of the interfacial area and interfacial velocity at σ = 57.8 mN/m, (b) on the correlation of interfacial area and interfacial velocity at σ = 25 mN/m, (c) on the mean interfacial velocity, and (d) on the ratio of static area.

3.6 *Effect of gas load*

In the preloading region, liquid flows freely onto the structured packing without any influence from the solvent. The selected gas loads in Table 1 fall in the preloading region. Therefore, it is anticipated that CDF curves of the fractional area will be similar for all five simulation cases. Fig. 9a illustrates very tight curves with minor differences. The mean interfacial velocities are shown in Fig. 9b. The variation is within 1 for the large range of gas loads and can be regarded as a fluctuation. Even though the effect of gas load is negligible in average sense like Fig. 9b, gas load still shows some importance on the ratio of static area in interfacial area as shown in Fig. 9c. The

variation in the ratio of static area is almost 0.05, the same as the effects of surface tension and contact angle. From this variation, the influence of gas load on static area cannot be overlooked. Fig. 9c shows a positive proportion of static area ratio and gas load. This is attributed to the resistance effect of gas flow on the liquid flow in the countercurrent flow. Higher gas load with larger momentum slows the interfacial velocity of the liquid. For thin-film flow with very small solvent velocity, this resistance would cause the fluid to stagnate and increase the static area. Gas load is expected to have a larger influence on film flow, rather than rivulet flow, in terms of static area.

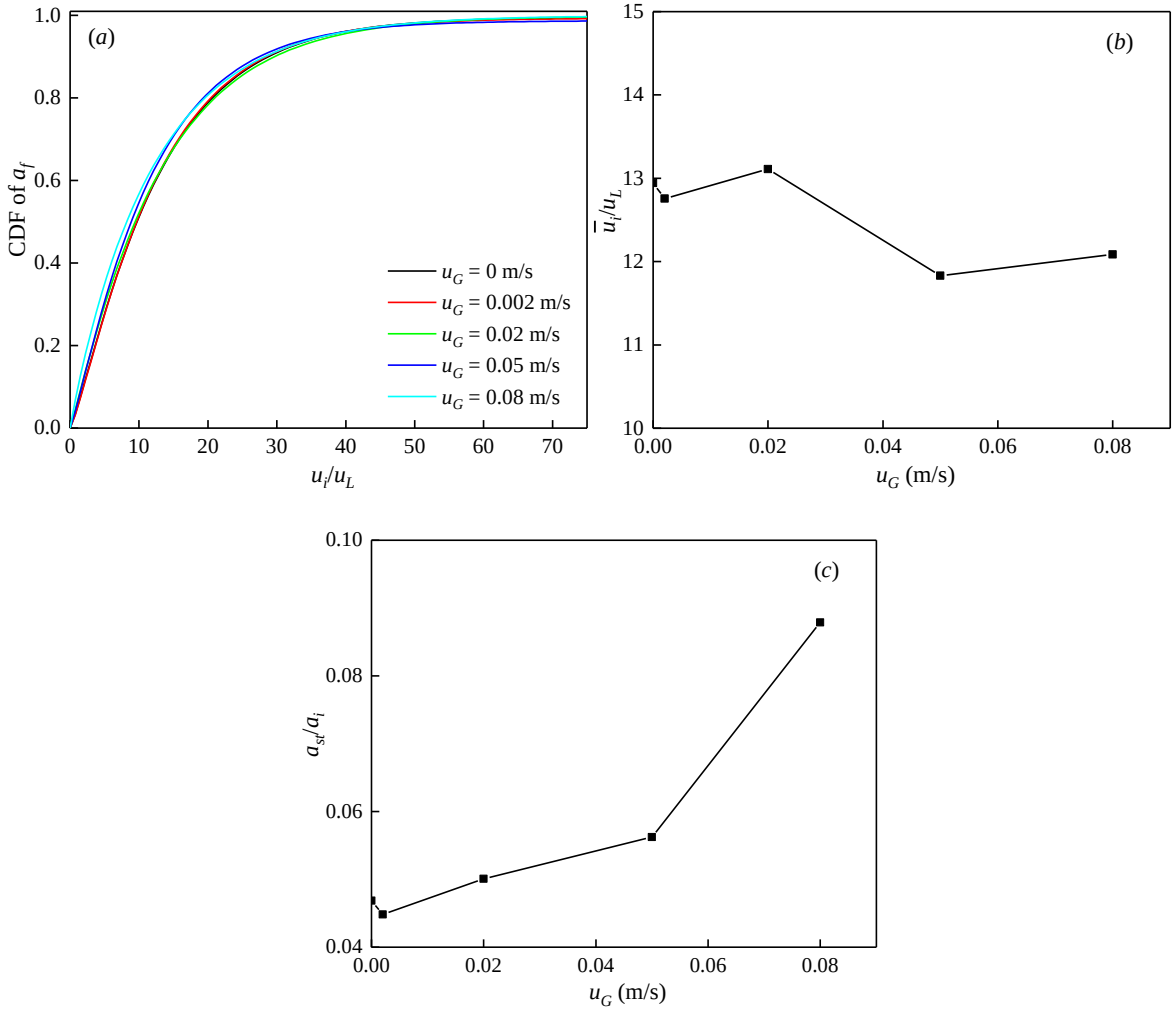

Fig. 9. The effect of gas load (a) on the correlation of interfacial area and interfacial velocity, (b) on the mean interfacial velocity, and (c) on the ratio of static area.

3.7 *Effect of liquid load*

Higher liquid load increases the kinetic energy of solvent flowing along the packing surface. Almost all correlations derived from both experiments and simulations predict the positive proportion of interfacial area and liquid load within certain ranges. However, it is not clear how the liquid load affects the interfacial velocity and the corresponding interfacial area. This section addresses this question by running six simulations (refer to Table 1). The correlation of fractional area and interfacial velocity is shown in Fig. 10a. With a higher liquid load, more of surface region presents higher interfacial velocity, which is expected. Note that the superficial velocity in individual case is used to normalize the interfacial velocity, rather than a constant value, to be consistent with the definition of static area. The correlation with respect to normalized interfacial velocity is shown in Fig. 10b. It shows that the case with relatively high superficial velocity presents high fraction of static area in comparison to case with low superficial velocity. It is attributed to the definition of static area which describes standard deviation to superficial velocity. The mean interfacial velocity follows a power law trend with liquid load, as shown in Fig. 10c. This trend can be qualitatively explained by Eq. (11)— the liquid load increases both the wetted area and the film thickness, and the relation $\bar{u}_i/u_L \propto \frac{1}{a_w \delta_L}$ shows power law function of u_L. This trend is depicted in Fig. 11, which shows the gas-liquid interface on the center packing sheet of the bottom unit. The figure shows that higher liquid load can cover more areas on the packing sheet, as is especially obvious in the middle valleys. The coloring also indicates a thicker liquid film at higher liquid loads. The liquid flows as rivulets along the packing channels and doesn't overcome the corrugation ridge of the packing layer. This flow pattern in Mellapak 500.Y is consistent with observation by 3D tomographic scans (Wehrli et al., 2018) and simulations (Olenberg and Kenig, 2017). The ratio of static area in interfacial area shows a increasing trend relative to liquid load, as shown in Fig. 10d. This can be interpreted from both Fig. 10b and 10c. Noted that this increasing trend is related to the fraction of static area, not the total static area. Another point is that the variation magnitudes of the static area ratio and mean interfacial velocity caused by the liquid load are much larger than other factors, like surface tension, contact angle, and gas load. The liquid load and viscosity impose similarly significant influences on the interfacial area.

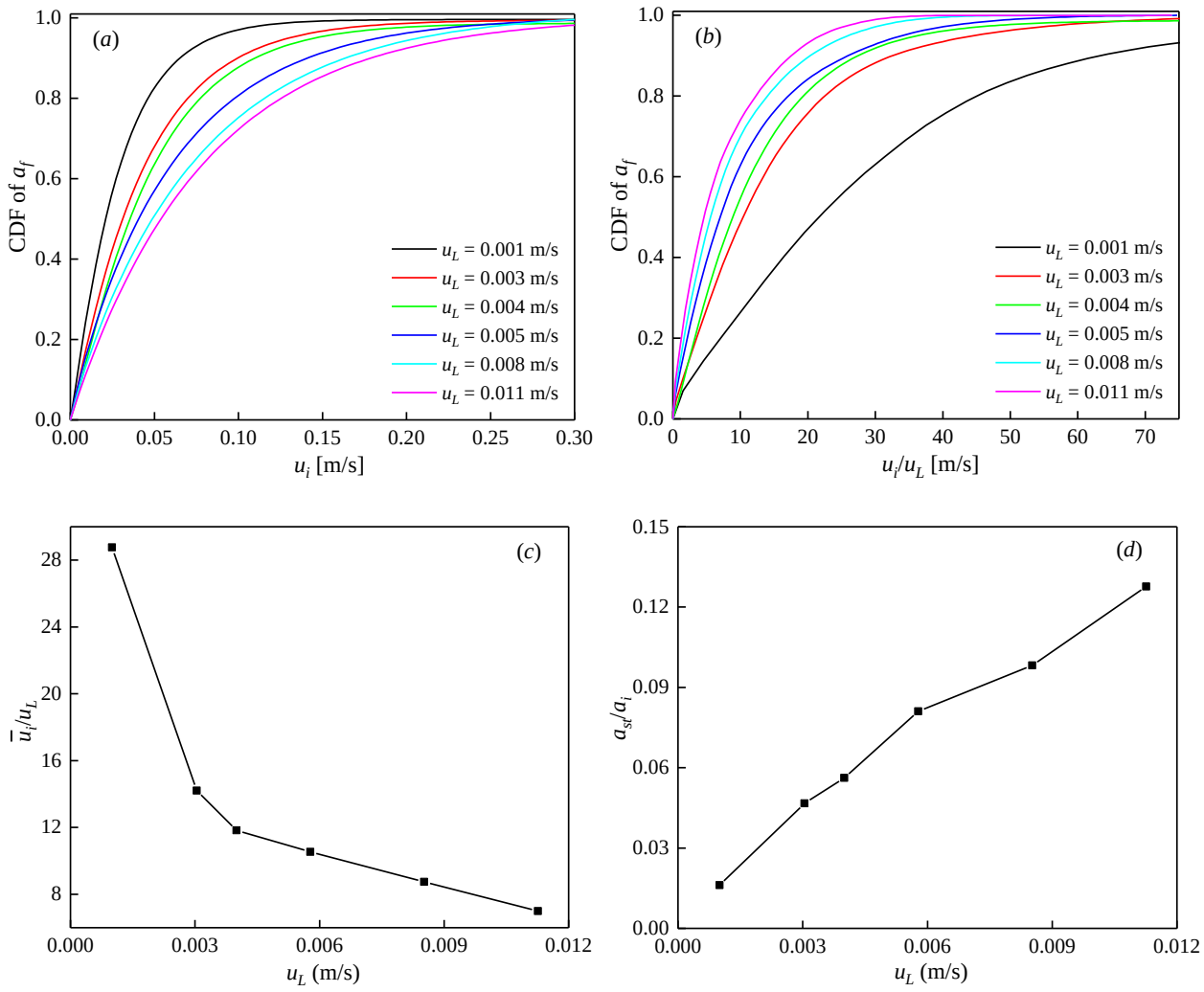

Fig. 10. The effect of liquid load (a) on the correlation of interfacial area and absolute interfacial velocity, (b) on the correlation of interfacial area and normalized interfacial velocity, (c) on the mean interfacial velocity, and (d) on the ratio of the static area. The *x* axis in (b) is cut to 75 to maintain clear visualization of curves.

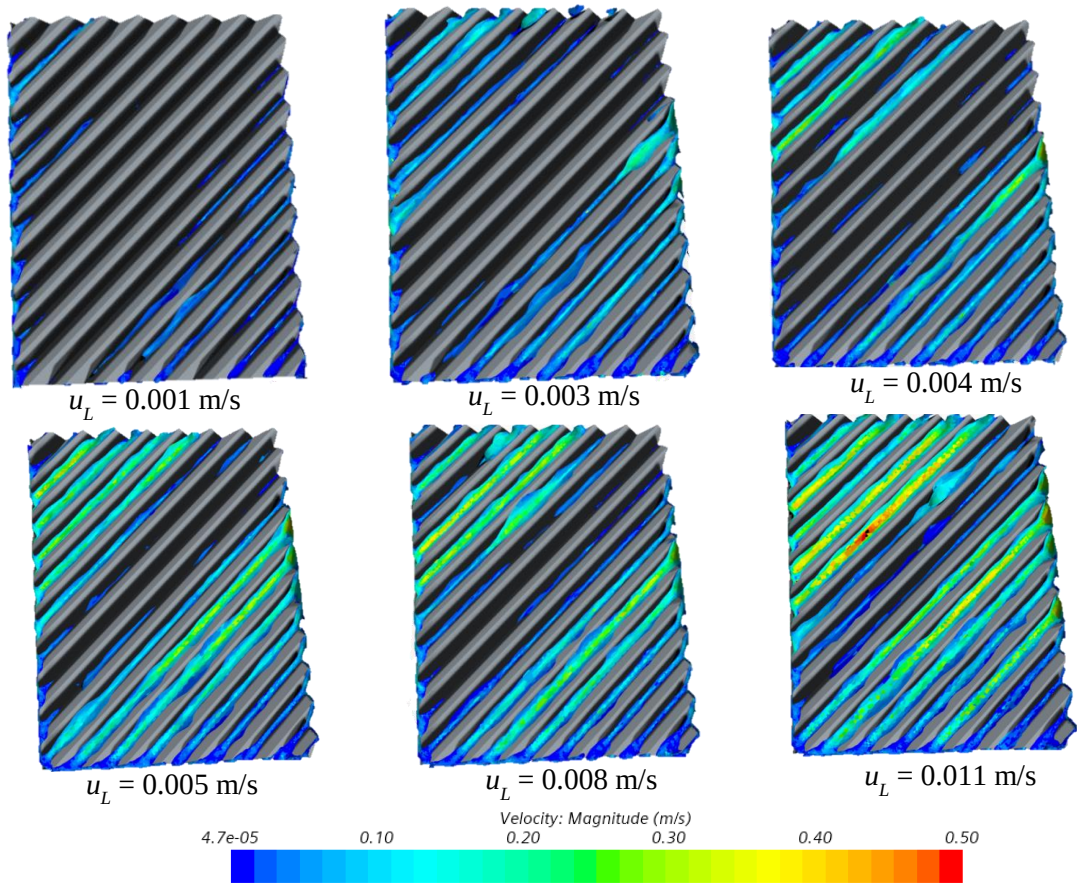

458

459 Fig. 11. Gas-liquid interface visualization on the center packing sheet of the bottom unit. The
460 interface is colorized by interfacial velocity magnitude.

461 3.8 *Effect of rotation angle*

462 In structured packing, gas and liquid flow through a single element and preferentially spread in a
463 series of packing units. To spread gas and liquid uniformly in all sheets, each packing unit is rotated
464 at a certain angle with respect to the adjacent element. This setup has been widely employed in
465 CO_2 capture in industrial applications. The rotation has been shown to increase the liquid holdup
466 and wetting area significantly (Fourati et al., 2012; Soulaine et al., 2014). Rotation also causes
467 fluid accumulation at the junction between adjacent packing elements because the packing channel
468 changes directions. X-ray tomography images showed that the global holdup at junctions is twice
469 as high as that in the interior of the packing unit (Toye et al., 2005). This creates additional
470 resistance to liquid and gas flow and then increases the gas flow pressure drop as the downside.
471 Consequently, the local liquid velocities slow down when crossing the element junctions. Pavlenko

et al. (2019) investigated the effect of rotation angle on the distribution of local liquid velocities in the packing cross section by experimental observation. With a higher rotational angle, the liquid velocity in the center of the packing cross section decreases, but the flow rate at the packing periphery increases. Hence, the uniformity of liquid flow increases. At θ_r = 90°, the flow is maximum at the periphery and minimum in the center compared to other rotations. Our simulation can substantiate their conclusion and provide more insights into static interfacial area.

The results for fractional areas at different rotation angles are shown in Fig. 12a. The curves are almost overlapping and show the minor influence of rotation angle on the interfacial velocity distribution. The mean interfacial velocity decreases at larger rotation angles, as shown in Fig. 12b. This decrease is due to the more significant dislocation (the rotation angle between upper unit and lower unit) of the flow channel from the upper unit to the lower unit and reduces the flow momentums. This can be confirmed by the gas-liquid interface visualization in Fig. 12e where the liquid velocity in diagonal longest channels reduces with larger rotation angles. Additionally, the entering velocity at metal sheet tip is smaller for case with larger rotation angle in Fig. 12e. This is also consistent with the conclusion drawn by Pavlenko et al. (2019). The fractional area increases at a larger rotation angle, as shown in Fig. 12c. This axial spreading of liquid increases and the original dry surface area becomes irrigated, increasing the fractional area of packing. In accordance with Eq. (11), the average interfacial velocity decreases and more area is likely to stagnate, as shown in Fig. 12e. This point is not discussed in the previous literature and reveals another downside of rotation, even though the variation in the static area is very slight, about 0.01. From the perspective of interfacial area, 90° is favorable given the underlying assumption that all interfacial area can contribute to mass transfer. However, the slightly increased ratio of static area undermines the advantage of higher interfacial area at 90° and needs to be considered for column design in combination of effectiveness of static area. Limited to current condition in this study, the packing with rotation angle of 90° would show better performance than those with other rotation angles.

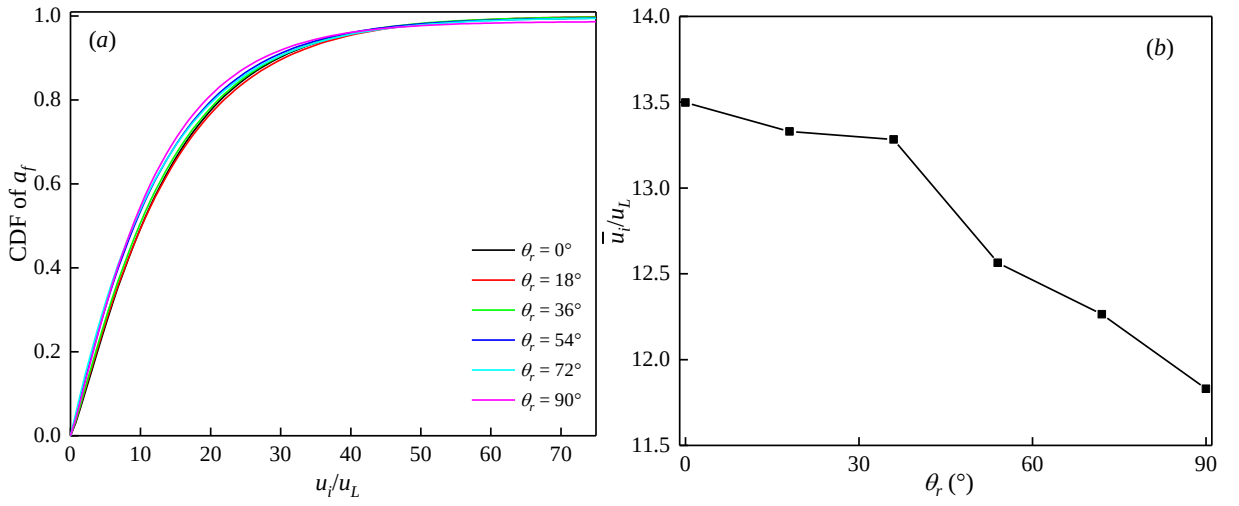
(a)
CDF of a_f
u_i/u_L
θ_r = 0°
θ_r = 18°
θ_r = 36°
θ_r = 54°
θ_r = 72°
θ_r = 90°
(b)
$\overline{u}_i/u_L$
θ_r (°)
(c)
a_f
θ_r (°)
(d)
a_{sf}/a_i
θ_r (°)

498

499

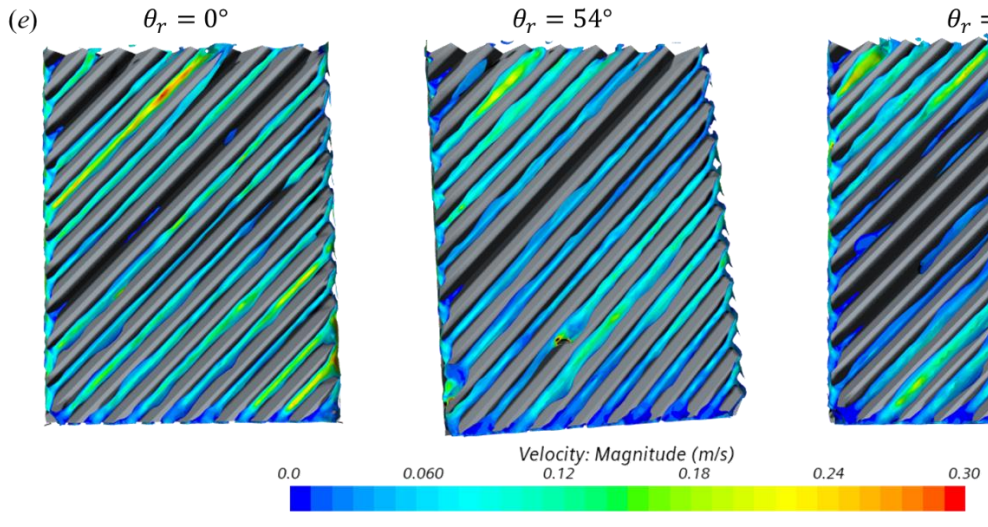
(e)
θ_r = 0°
θ_r = 54°
θ_r = 90°
Velocity: Magnitude (m/s)
0.0
0.060
0.12
0.18
0.24
0.30

500

Fig. 12. The effect of rotation angle on (a) the relationship between interfacial area and interfacial velocity, (b) the mean interfacial velocity, (c) the fractional area, (d) the ratio of static area, and (e) gas-liquid interface visualization at bottom unit for three rotation angles.

4. Discussion

In addition to the static interfacial area, the effects of the aforementioned factors on the total interfacial area are also discussed and compared with existing correlations. The current data set also is compared with existing correlations of the static area and holdup, and the merits of current work are discussed as well. The effects of these factors on static area and mean interfacial velocity are discussed to highlight the factors whose influence is dominant. The practical application of current work is discussed as well.

4.1 *In Comparison with existing correlation of fractional area*

Numerous correlations have been proposed to predict the fractional area in the packed column (Wang et al., 2005). Many are derived from chemical absorption/mass-transfer measurements, because direct measurement of fractional area is difficult in experiments. The latest relevant correlation proposed by Song et al. (2018) is used to compare with simulation data. The fractional area is calculated based on the volumetric mass-transfer rate and measured mass-transfer coefficient as follows (Song et al., 2018):

$$a_f = 1.16\eta \left[\frac{\rho_L}{\sigma} g^{1/2} u_L a_p^{-3/2}\right]^{0.138} \tag{12}$$

where η is a coefficient that depends on the packing type, surface materials, and loading condition. For the structured packing and preloading condition in this study, η is 1.0 for stainless steel and 0.62 for plastic surface. The contact angle is implicitly represented by this coefficient because Eq. (12) does not have a term representing the contact angle. In addition, Song et al. (2018) treated other factors considered in our analysis (but not in Eq. (12)), such as viscosity and gas load, as insignificant relative to fractional area. The relative error for insignificance is 10%.

The effects of solvent properties, gas, and liquid loads on the fractional area were presented separately in the previous section. To clearly illustrate their relative importance, the y axis in all figures is fixed to 0 and 1. The correlation and CFD data are compared in Fig. 13.

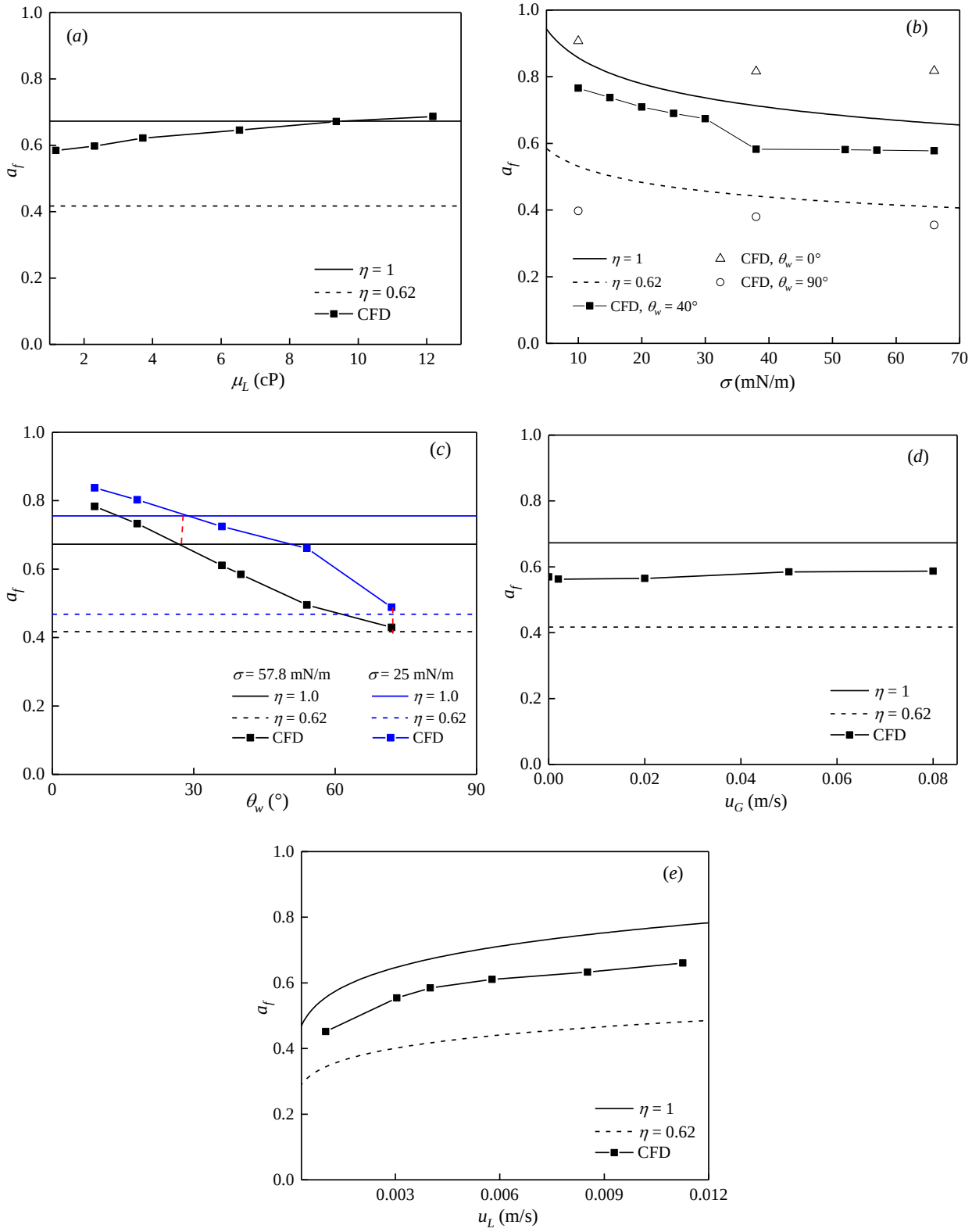

Fig. 13. Comparison of fractional area by correlation and CFD simulation showing the effects of (a) viscosity, (b) surface tension, (c) contact angle, (d) gas load, and (e) liquid load.

Because η varies with surface texture, both curves representing metal (η = 1) and plastic (η = 0.62) surfaces are plotted in the graphs. Fig. 13a shows the influence of viscosity on fractional area. a_f has a variation of 0.1 in the specified viscosity range, which cannot be treated as negligible. The average dependence of a_f on μ_L by Song et al. (2018) is -0.007 $\mp$ 0.022, whereas it is about 0.07 in our simulation. This difference may be attributed to the experimental measurement in Eq. (12) because it is impossible to only vary viscosity without changing other physical properties for the measurement of gas-liquid interfacial area with chemical absorption. It is admitted that the investigated liquid rate in Song et al. (2018) ranges 6-73 m^3/m^2h which shows wider range and higher load than 14.4 m^3/m^2h for base case in our study. The interfacial area is found to increase with liquid viscosity by X-ray measurement on Mellapak structured packing (Janzen et al., 2013). X-ray measuring technique can overcome the interdependence of physical properties in interfacial area measurement since the impact of liquid system properties on mass transfer phenomena is irreverent for X-ray tomography. Their measurement with liquid load ranging 4-25 m^3/m^2h can confirm our relation between interfacial area and liquid viscosity in Fig. 13*a*. In addition, predictions concerning the influence of viscosity in existing correlations conflict with one another. Some correlations stated a positive dependence of the fractional area on viscosity (Bravo and Fair, 1982; Rizzuti et al., 1981; Singh et al., 2018), other predicted negative dependence (Brunazzi et al., 1995; De Brito et al., 1994), and the rest predicted no dependence (Rocha et al., 1993; Tsai, 2010).

The effect of surface tension on fractional area is shown in Fig. 13b. The simulation curve with θ_w = 40°, which is the same as the base case, falls between correlation curves and exhibits the same trend. It validates the consistency of our simulation with experimentally derived correlation Eq. (12). Because the contact angle is embedded in η, η = 1 and η = 0.62 represent the highly wetting and weakly wetting properties of metal and plastic surfaces, respectively. That is, η = 1 corresponds to small θ_w and η = 0.62 corresponds to large θ_w based on the negative dependence of the fractional area on the contact angle. To determine the upper and lower bounds of this dependence, two additional sets of simulations with θ_w = 0° and θ_w = 90° are run. The data with θ_w = 0° lie above the curve with η = 1 and the data with θ_w = 90° lie below the curve with η = 0.62. This further validates our simulation. The simulation data also show that the limiting fractional area with θ_w = 0° is always above 0.8 and that with θ_w = 90° it is around 0.4, irrespective of the surface tension.

These data provide additional information about the limiting condition of the fractional area at different contact angles and surface tensions.

The effect of contact angle at two surface tensions is shown in Fig. 13c. The a_f reductions for θ_w from 9° to 72° are very close for two curves as well as the curve slopes, which indicates the independent relationship between contact angle and surface tension. Comparison of the a_f drops in Fig. 13b and 13c, it indicates that contact angle overperforms surface tension relative to the influence of the fractional area. One interesting point is the concurrent crossing of the CFD curve by the correlation lines, marked by the red dashed lines. The crossing can roughly estimate the contact angles of 27° and 75° corresponding to η = 1.0 and η = 0.62, respectively, and the angles are both in a reasonable range for metal and plastic surface and consistent with all graphs in Fig. 13. With this information, the correlation in Eq. (12) can more accurately predict the fractional area and make the comparison with other emergent data.

The effects of gas and liquid loads are illustrated in Fig. 13d and 13e. They show a negligible effect of gas load and a significant effect of liquid load, consistent with the conclusion represented by Eq. (12). The trend of a_f with respect to u_L for simulation is almost the same as that for correlation.

Overall, the simulation exhibits good agreement with the latest correlation of fractional area in terms of liquid properties and loading conditions. The only difference is for the effect of viscosity. Viscosity is a long-lasting conflicting factor in literature and needs more investigation. In this sense, our CFD model is validated by the experimentally derived correlation. It also presents the capability to back out the uncertain parameters in correlations, like contact angle corresponding to η.

4.2 *Dependence of static area*

The prediction correlation of the static area indicates the importance of ruling out inactive area from interfacial area in the calculation of effective area. Puranik and Vogelpohl (1974) provided the only existing correlation for static area derived from statistical analysis of various previous experimental data. After adjustment to our notations, their correlation for static area is as follows:

$$\frac{a_{st}}{a_i} a_f = 0.229 - 0.091 ln\left(\frac{\rho_L g}{\sigma a_p^2}\right) \tag{13}$$

where the static area is expressed as the ratio of the total surface area, rather than the ratio of interfacial area as done in Section 3. It shows that only surface tension influences in all specified physical properties. In addition, the static area calculated by Eq. (13) for the base case is about 0.264. That means, one quarter of the total surface area is covered by stagnant film. The negligible influence of liquid load in Eq. (13) contradicts other experimental measurements (Gelbe, 1968; Schubert et al., 1986) that indicate static area decreases with higher liquid loads. Their experiments also show the effect of viscosity on static area. In this aspect, the correlation for static area needs further analysis.

Our simulation provides insights into the dependence of static area on the discussed factors. The static area is defined as the ratio of the total surface area: $a_{st} \cdot a_f / a_i$. It shows a positive dependence on viscosity, independent of surface tension, negative dependence on the contact angle term ($1-\cos\theta_w$), weakly positive dependence on gas load, and negative dependence on liquid load. The dependence on viscosity, contact angle, and liquid load cannot be overlooked. A more extensive data set is need to the determine the specific form of this dependence and the associated correlation.

4.3 *Relative importance of discussed factors*

The influence of six factors on the static and fractional areas are presented separately in Section 3 and 4.1. Note that the effective mass-transfer area depends on both areas, and hence the comprehensive evaluation of the impacts of the factors on the effective area requires a combination of both metrics (static area and fractional area). Because the specified ranges of physical properties and loading conditions cover prevalent solvents and operating conditions, the variations in static area and fractional area corresponding to those ranges can represent the dominance of an individual factor in the effective mass-transfer area. Therefore, the variations in the static area and fractional area in the previous sections are collectively shown in Fig. 14. Fig. 14a illustrates the significant influence of viscosity on the static area. Surface tension, contact angle, gas load, and liquid load have similar influences on the static area. The rotation angle has the least influence. From this perspective, the influence of viscosity is underestimated by most existing correlations because few investigators have endeavored to analyze the percentage of the static area. This study emphasizes the value of evaluating the relative importance of the six factors and highlights the influence of viscosity. Comparison of the influence of the factors on the fractional area in Fig. 14b reveals the dominant influence of contact angle, which is consistent with existing understandings (Rocha et

al., 1993; Shi and Mersmann, 1985; Singh et al., 2016). The influence of surface tension and liquid load on the fractional area are of secondary importance. The gas load and rotational angle have negligible influences on the fractional area.

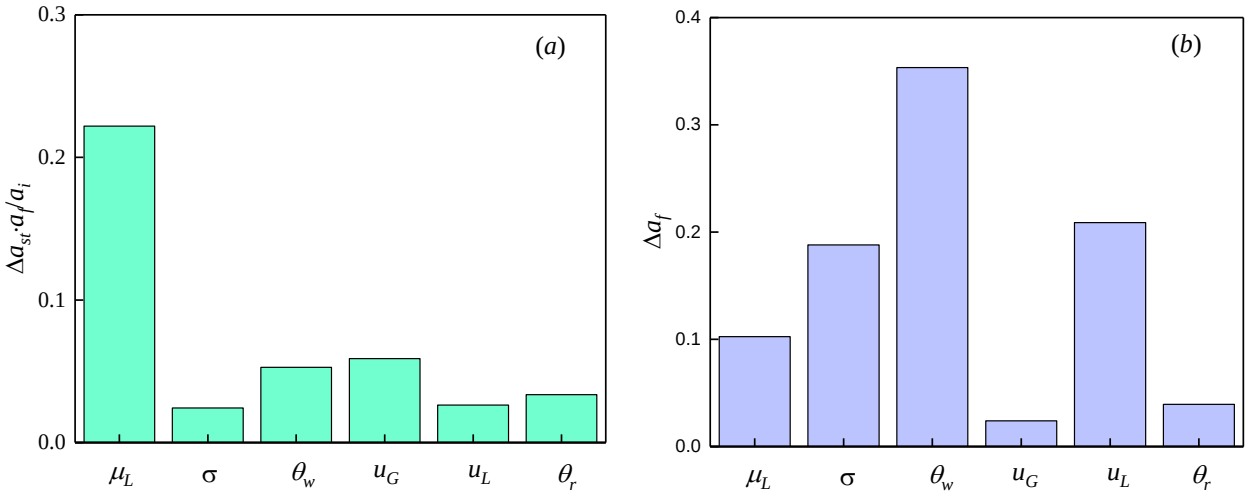

Fig. 14. The variation of (a) static area and (b) fractional area in the specified range of discussed factors in Table 1.

4.4 *In comparison with existing correlation of holdup*

Besides the comparison of fractional area with latest correlation in section 4.1, the liquid holdup is also compared with well-established correlation in an effort to assess the reliability of current CFD model. Many empirical correlations are derived to predict liquid holdup in Mellapak structured packing columns (Olujić et al., 2007; Rocha et al., 1993; Stichlmair et al., 1989; Suess and Spiegel, 1992). The well-established correlation by Suess and Spiegel (1992) will be used to compare with our CFD results. The predictive holdup correlation is,

$$h_L = c\left(\frac{a_p}{V}\right)^{0.83} B^x \left(\frac{\mu_L}{\mu_0}\right)^{0.25} \tag{14}$$

with c = 0.0169 and x = 0.37 for B < 40 m^3/m^2h and c = 0.0075 and x = 0.59 for B > 40 m^3/m^2h. V is the volume of packing column, μ_0 is the dynamic viscosity of water at 20°C. Liquid holdup is calculated in Eq. (14) as a function of liquid load, liquid viscosity, and specific surface area of the packing. The dependances of liquid holdup on liquid viscosity and superficial velocity are compared between CFD result and Eq. (14), as shown in Fig. 15. Overall, good agreement is reached between CFD result and correlation in Eq. (14). It is noted that some increasing minor

difference still exists between CFD results and existing correlation with larger liquid viscosity and superficial velocity. It is due to difference of power law dependence on viscosity and velocity. The power exponents of viscosity and low velocity in Eq. (14) are 0.37 and 0.25, respectively. The fitted power exponents of viscosity and velocity from CFD results are 0.29 and 0.19, respectively. Several possible interpretations can tell this difference. Firstly, the correlation in Eq. (14) is derived based on the structured packing (Mellapak 250.X, Mellapak 250.Y and 500.Y). Least square regression is applied on all data to obtain the power exponents. Some variation would exist for Mellapak 500.Y, which will cause some difference of power exponents. Most likely interpretation is the slight difference of packing structure in this study and Eq. (14). Wiper band and surface texture (embossing and perforation) are not considered for our geometry in Fig. 1(a). The static holdup at contact points between adjacent packing sheets usually takes 1% to 2% of total holdup (Aferka et al., 2011; Rocha et al., 1993), which can cause the difference between our results and correlation in Eq. (14). The smaller holdup on smooth structured packing with no holes than industrial packing is confirmed as well by Schug and Arlt (2016). The smaller power exponent of velocity than correlation in Eq. (14) is also observed by Olujić et al. (2007). Additionally, it is noted that only effects of velocity and viscosity are considered in Eq. (14). Complicated correlation for liquid holdup also shows dependence on crimp angle of corrugation and contact angle etc. (Rocha et al., 1993).

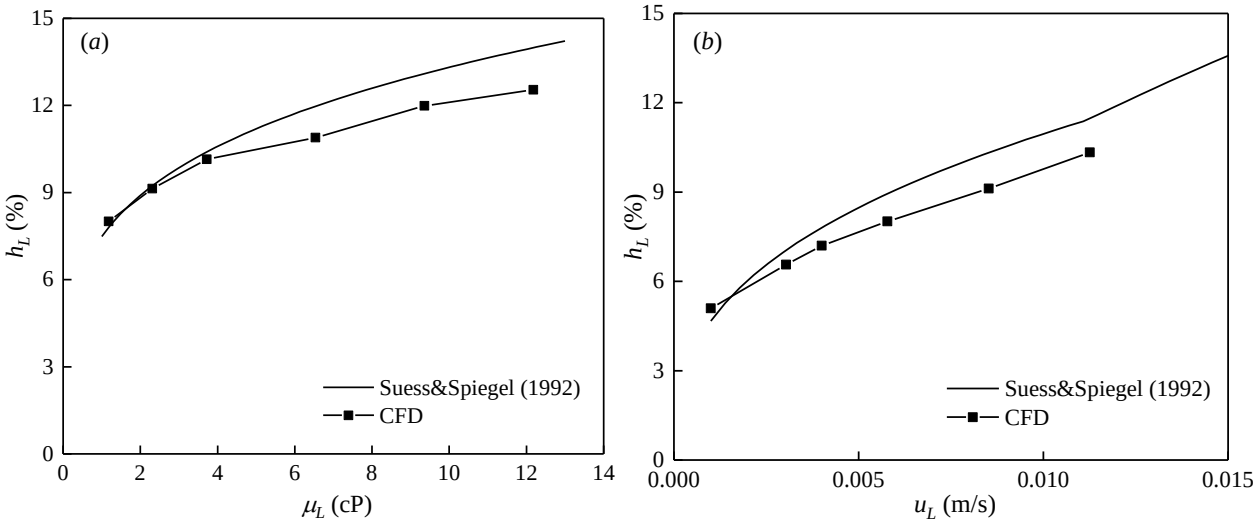

Fig. 15. Comparison of overall holdup in Mellapak 500.Y between CFD results and existing correlation with respect to (a) viscosity and (b) superficial liquid velocity.

4.5 *Practical application discussion*

In this study, the static area and dynamic area are differentiated in interfacial area. It provides insight on the uncertainty analysis of existing correlation for fractional area since most correlations do not separate static area from interfacial area or interchangeably use interfacial area and effective area. It also offers alternative method to construct more accurate empirical correlation of fractional area. Some discussions are followed about the practical application of current model and results. Compared to practical packing column, the constructed geometry in this study maintains the core features and ignores some other features, i.e., wiper band and surface textures. Wiper bands are wrapped around the circumference of the element and bent toward the column wall prior to installing the packing. It helps direct liquid flow back into the packing element and prevent gas channeling. In the section with wiper bands, the porosity decreases and surface area increases, enhanced liquid accumulation is observed via X-ray CT near wiper bands, and lower away from wiper bands (Aferka et al., 2011; Owens et al., 2009). Additionally, the contact between adjacent packing sheets confined by wiper bands also results in local accumulation of liquid (Janzen et al., 2013). The liquid at those contact points is continuously renewed by the liquid flow and liquid mixing is promoted. The liquid holdup at those contact points are measured ranging between 1% and 2% (Aferka et al., 2011). Therefore, the presence of wiper band would increase the interfacial area, but the quantification of enhancement needs future analysis. Surface texture (embossing) shows multiscale roughness from microscale to millimeter scale, and is difficult to fully resolve those multiscale features in simulation (Nicolaiewsky and Fair, 1999). The simplified pattern of surface texture is considered in simulation to show enhanced wetted area (Sebastia-Saez et al., 2013). This enhanced interfacial area is also confirmed with experimental measurement (Tsai, 2010). Perforation on practical metal sheet in structured packing help equalize radial pressure profiles in the packing column and to promote liquid spreading. The presence of perforations enhances wetting and increases the contact area for liquid gas interaction at low flow rate regime where liquid crosses the holes to wet the other side of perforated sheets (Subramanian and Wozny, 2012). At high flow rate regime, the effect of perforation is negligible due to hole covered by liquid. Aforementioned factors increase interfacial area and cause deviation from prediction by current model and results.

5. Conclusion

Post-combustion carbon capture via solvent absorption has attracted significant interest among industry and scientific research communities due to its prospective deployment in the mitigation of greenhouse gas emissions. The design of absorption columns relies highly on the prediction of the mass-transfer coefficient and effective mass-transfer area. The accurate prediction of the effective area depends on both static area and interfacial area. In this study, a 3-D multiphase simulation using the VOF method was conducted to investigate the interfacial area, especially the static area. The two-packing unit Mellapak 500.Y structured packing was analyzed because of its commercial deployment by industry. A wide range of physical properties—viscosity, surface tension, contact angle, gas load, liquid load, and rotation angle—were considered in the analysis.

The correlation of interfacial area and interfacial velocity at the local scale can be described by gamma distribution, which can capture velocity distribution at the gas-liquid interface and be used to describe the static area percentage in the interfacial area. Assuming a given velocity threshold, the static area percentage for different physical properties can be quantified. It shows the significant influence of viscosity on static area, which is usually ignored in existing literature. In addition, the interfacial area at different physical properties is compared with existing correlations and shows good agreement to validate the current CFD model.

The issue of current correlation for the static area is also discussed and the approach in this study provides a means of more accurately establishing the correlation for the static area. Viscosity is the dominant influence on static area, and contact angle the main effect on interfacial area. In the prediction of effective area, both factors need special attention to obtain accurate results. Since contact angle has the most pronounced influence on predicted interfacial area, its experimental determination is very critical. Conventionally, the sessile drop technique is employed to determine static contact angle on flat plate. However, the textured packing sheet makes the measurement complicated and far from accuracy. Wilhemy plate technique can be used to measure effective contact angle and provide more accurate key parameter for simulation and correlations. Relevant progress on the contact angle measurement will come out soon.

The effectiveness of the static area relative to mass transfer also needs to be better understood and will be analyzed in further study to accurately predict the effective area.

Acknowledgement

Pacific Northwest National Laboratory is operated by Battelle for the U.S. Department of Energy (DOE) under Contract No. DEAC05-76RL01830. This work was funded by the DOE Office of Fossil Energy's Carbon Capture Simulation Initiative (CCSI) through the National Energy Technology Laboratory.

NOMENCLATURE

Roman Letters

A = cross-sectional area of packing column, m^2

A_{in} = cross-sectional area of dripping points, m^2

A_{out} = area of outlet boundary of packing column, m^2

a_e = effective area, m^2

a_w = wetted area, m^2

a_i = interfacial area, m^2

a_{st} = static part of interfacial area, m^2

a_{dyn} = dynamic part of interfacial area, m^2

a_f = fractional area, $a_f = a_e/a_p$

a_p = geometric area of packing surface, m^2

B = liquid load, m^3/m^2h

c = factor in Eq. (13)

$C_{CO_2,in}$ = inlet CO_2 concentration in packing column, mol/m^3

$C_{CO_2,out}$ = outlet CO_2 concentration in packing column, mol/m^3

F = surface tension force at the gas-liquid interface per unit volume, N/m^3

g = gravity acceleration, m/s^2

h_L = liquid holdup, %

h = height of packing column, m

k'_g = liquid film mass transfer coefficient, $kmol/m^2 \cdot Pa \cdot s$

R = ideal gas constant, 8314.5 $m^3 \cdot Pa/kmol \cdot K$

T = temperature, K

u = velocity vector of effective fluid, m/s

$u_{L,in}$, $u_{G,out}$ = inlet velocity at the liquid distributor and outlet velocity of gas at top boundary, m/s

u_L, u_G = liquid and gas superficial velocity, m/s

u_i, $\overline{u_i}$ = local and averaged interfacial velocity of liquid, m/s

x = exponent of liquid load in Eq. (13)

V = volume of two-unit packing column, m^3

Greek Letters

α = volume fraction of liquid phase

μ = dynamic viscosity of fluid, mPa·s

χ = effective part of a_{st}

ρ = density of fluid, kg/m^3

σ = interfacial tension, mN/m

δ_L = mean film thickness, m

θ_w = contact angle at the three-phase contact line, °

θ_r = rotation angle between two units of packing column, °

Γ() =gamma function

γ(,) = lower incomplete gamma function

η = coefficient related to material types

Dimensionless Groups

Ha = Hatta number

Subscript

i = gas-liquid interfacial variable

n = normal component of a vector

s = tangential component of a vector

L = liquid component

G = gas component

References

Aferka, S., Viva, A., Brunazzi, E., Marchot, P., Crine, M., Toye, D., 2011. Tomographic measurement of liquid hold up and effective interfacial area distributions in a column packed with high performance structured packings. Chemical Engineering Science 66, 3413-3422.

Baldi, G., Sicardi, S., 1975. A model for mass transfer with and without chemical reaction in packed towers. Chemical Engineering Science 30, 617-624.

Basden, M., Eldridge, R.B., Farone, J., Feng, E., Hussey, D.S., Jacobson, D.L., 2013. Liquid holdup profiles in structured packing determined via neutron radiography. Industrial & engineering chemistry research 52, 17263-17269.

Basden, M.A., 2014. Characterization of structured packing via computational fluid dynamics.

Bird, R.B., Stewart, W.E., Lightfoot, E.N., 2006. Transport phenomena. John Wiley & Sons.

Brackbill, J.U., Kothe, D.B., Zemach, C., 1992. A continuum method for modeling surface tension. Journal of computational physics 100, 335-354.

Bravo, J.L., Fair, J.R., 1982. Generalized correlation for mass transfer in packed distillation columns. Industrial & Engineering Chemistry Process Design and Development 21, 162-170.

Brunazzi, E., Nardini, G., Paglianti, A., Petarca, L., 1995. Interfacial area of mellapak packing: Absorption of 1, 1, 1-trichloroethane by Genosorb 300. Chemical Engineering & Technology: Industrial Chemistry-Plant Equipment-Process Engineering-Biotechnology 18, 248-255.

Cai, T., 2018. Pour Point Density Estimations for Packed Columns with Structured Packings. CHEMICAL ENGINEERING 69.

CD-adapco, 2020. STAR-CCM+ 15.02 User Guide. CD-adpco Inc., NY, USA.

Danckwerts, P., 1970. Chemical methods of measuring interfacial area and mass transfer coefficients in two-fluid systems. Brit. Chem. Eng. 15, 522-526.

De Brito, M.H., Von Stockar, U., Bangerter, A.M., Bomio, P., Laso, M., 1994. Effective mass-transfer area in a pilot plant column equipped with structured packings and with ceramic rings. Industrial & engineering chemistry research 33, 647-656.

Fourati, M., Roig, V., Raynal, L., 2012. Experimental study of liquid spreading in structured packings. Chemical Engineering Science 80, 1-15.

Fu, Y., Bao, J., Singh, R., Wang, C., Xu, Z., 2020a. Investigation of countercurrent flow profile and liquid holdup in random packed column with local CFD data. Chemical Engineering Science 221, 115693.

Fu, Y., Bao, J., Wang, C., Singh, R.K., Barpaga, D., Zheng, R.F., Xu, Z., Bhat, S., Baca, J., Anderson-Cook, C., 2020b. Absorber Column CFD model validation against PNNL's device-scale absorber column on the LCFS unit. Pacific Northwest National Lab.(PNNL), Richland, WA (United States).

Gelbe, H., 1968. A new correlation for liquid holdup in packed beds. Chemical Engineering Science 23, 1401-1403.

Green, C.W., Farone, J., Briley, J.K., Eldridge, R.B., Ketcham, R.A., Nightingale, B., 2007. Novel application of X-ray computed tomography: Determination of gas/liquid contact area and liquid holdup in structured packing. Industrial & engineering chemistry research 46, 5734-5753.

Hegely, L., Roesler, J., Alix, P., Rouzineau, D., Meyer, M., 2017. Absorption methods for the determination of mass transfer parameters of packing internals: A literature review. AIChE Journal 63, 3246-3275.

Janzen, A., Steube, J., Aferka, S., Kenig, E., Crine, M., Marchot, P., Toye, D., 2013. Investigation of liquid flow morphology inside a structured packing using X-ray tomography. Chemical Engineering Science 102, 451-460.
Joosten, G., Danckwerts, P., 1973. Chemical reaction and effective interfacial areas in gas absorption. Chemical Engineering Science 28, 453-461.
Muzaferija, S., 1998. Computation of free surface flows using interface-tracking and interface-capturing methods. Nonlinear water-wave interaction. Computational Mechanics, Southampton.
Nakajima, E.S., Maffia, M.C., Meirelles, A.J., 2000. Influence of liquid viscosity and gas superficial velocity on effective mass transfer area in packed columns. Journal of chemical engineering of Japan 33, 561-566.
Nicolaiewsky, E.M., Fair, J.R., 1999. Liquid flow over textured surfaces. 1. Contact angles. Industrial & engineering chemistry research 38, 284-291.
Olenberg, A., Kenig, E.Y., 2017. Numerical simulation of two-phase flow in representative elements of structured packings, Computer Aided Chemical Engineering. Elsevier, pp. 2089-2094.
Olujić, Ž., 1999. Effect of column diameter on pressure drop of a corrugated sheet structured packing. Chemical Engineering Research and Design 77, 505-510.
Olujić, Ž., Behrens, M., Spiegel, L., 2007. Experimental characterization and modeling of the performance of a large-specific-area high-capacity structured packing. Industrial & engineering chemistry research 46, 883-893.
Owens, S.A., Kossmann, A., Farone, J., Eldridge, R.B., Ketcham, R.A., 2009. Flow field visualization in structured packing using real time X-ray radiography. Industrial & engineering chemistry research 48, 3606-3618.
Patwardhan, V.S., 1979. The effectiveness of static hold-up for absorption with a chemical reaction in a packed trickle bed: General order kinetics. The Canadian Journal of Chemical Engineering 57, 582-585.
Pavlenko, A., Pecherkin, N., Zhukov, V., Meski, G., Houghton, P., 2020. Overview of methods to control the liquid distribution in distillation columns with structured packing: Improving separation efficiency. Renewable and Sustainable Energy Reviews 132, 110092.
Pavlenko, A., Pecherkin, N., Zhukov, V., Nazarov, A., Meski, G., Houghton, P., 2019. Effect of the angle of rotation of structured packing layers on separation efficiency in distillation column, Journal of Physics: Conference Series. IOP Publishing, p. 012036.
Puranik, S., Vogelpohl, A., 1974. Effective interfacial area in irrigated packed columns. Chemical Engineering Science 29, 501-507.
Rao, A.B., Rubin, E.S., 2002. A technical, economic, and environmental assessment of amine-based CO2 capture technology for power plant greenhouse gas control. Environmental science & technology 36, 4467-4475.
Rizzuti, L., Augugliaro, V., Cascio, G.L., 1981. The influence of the liquid viscosity on the effective interfacial area in packed columns. Chemical Engineering Science 36, 973-978.
Rocha, J.A., Bravo, J.L., Fair, J.R., 1993. Distillation columns containing structured packings: a comprehensive model for their performance. 1. Hydraulic models. Industrial & engineering chemistry research 32, 641-651.
Rocha, J.A., Bravo, J.L., Fair, J.R., 1996. Distillation Columns Containing Structured Packings: A Comprehensive Model for Their Performance. 2. Mass-Transfer Model. Industrial & engineering chemistry research 35, 1660-1667.
Rochelle, G.T., 2009. Amine scrubbing for CO2 capture. Science 325, 1652-1654.
Schubert, C., Lindner, J., Kelly, R., 1986. Experimental methods for measuring static liquid holdup in packed columns. AIChE Journal 32, 1920-1923.
Schug, S., Arlt, W., 2016. Imaging of fluid dynamics in a structured packing using X-ray computed tomography. Chemical Engineering & Technology 39, 1561-1569.

Sebastia-Saez, D., Gu, S., Ranganathan, P., Papadikis, K., 2013. 3D modeling of hydrodynamics and physical mass transfer characteristics of liquid film flows in structured packing elements. International Journal of Greenhouse Gas Control 19, 492-502.
Shi, M., Mersmann, A., 1985. Effective interfacial area in packed columns.
Shulman, H., Ullrich, C., Wells, N., 1955. Performance of packed columns. I. Total, static, and operating holdups. AIChE Journal 1, 247-253.
Singh, R.K., Bao, J., Wang, C., Fu, Y., Xu, Z., 2020. Hydrodynamics of countercurrent flows in a structured packed column: Effects of initial wetting and dynamic contact angle. Chemical Engineering Journal 398, 125548.
Singh, R.K., Galvin, J.E., Sun, X., 2016. Three-dimensional simulation of rivulet and film flows over an inclined plate: Effects of solvent properties and contact angle. Chemical Engineering Science 142, 244-257.
Singh, R.K., Galvin, J.E., Sun, X., 2018. Multiphase flow studies for microscale hydrodynamics in the structured packed column. Chemical Engineering Journal 353, 949-963.
Singh, R.K., Galvin, J.E., Whyatt, G.A., Sun, X., 2017. Breakup of a liquid rivulet falling over an inclined plate: Identification of a critical Weber number. Physics of Fluids 29, 052101.
Song, D., Seibert, A.F., Rochelle, G.T., 2018. Mass transfer parameters for packings: effect of viscosity. Industrial & engineering chemistry research 57, 718-729.
Soulaine, C., Horgue, P., Franc, J., Quintard, M., 2014. Gas–liquid flow modeling in columns equipped with structured packing. AIChE Journal 60, 3665-3674.
Stichlmair, J., Bravo, J., Fair, J., 1989. General model for prediction of pressure drop and capacity of countercurrent gas/liquid packed columns. Gas Separation & Purification 3, 19-28.
Subramanian, K., Wozny, G., 2012. Analysis of hydrodynamics of fluid flow on corrugated sheets of packing. International Journal of Chemical Engineering 2012.
Suess, P., Spiegel, L., 1992. Hold-up of Mellapak structured packings. Chemical Engineering and Processing: Process Intensification 31, 119-124.
Toye, D., Crine, M., Marchot, P., 2005. Imaging of liquid distribution in reactive distillation packings with a new high-energy X-ray tomograph. Measurement Science and Technology 16, 2213.
Tsai, R.E., 2010. Mass transfer area of structured packing.
Tsai, R.E., Schultheiss, P., Kettner, A., Lewis, J.C., Seibert, A.F., Eldridge, R.B., Rochelle, G.T., 2008. Influence of surface tension on effective packing area. Industrial & engineering chemistry research 47, 1253-1260.
Wang, G., Yuan, X., Yu, K., 2005. Review of mass-transfer correlations for packed columns. Industrial & engineering chemistry research 44, 8715-8729.
Wehrli, M., Kögl, T., Linder, T., Arlt, W., 2018. An unobstructed view of liquid flow in structured packing. Chem. Eng 69, 775-780.